TECHNISCHE UNIVERSITÄT WIEN
Vienna University of Technology

D I P L O M A R B E I T

Simulationsstudie zur Ausscheidungs- und Mikrostrukturentwicklung in Ni-Basis-Superlegierungen

Ausgeführt am Institut für

Werkstoffwissenschaften und Werkstofftechnologie

der Technischen Universität Wien

unter der Anleitung von

Univ.-Prof. Dipl.-Ing. Dr.techn. Ernst Kozeschnik

und

Dipl.-Ing. Markus Rath

durch

Philipp Retzl, BSc

[redacted]

_____ _____

Datum Unterschrift

Abstract

Modern nickel-base Superalloys are complex, multiphase materials for high temperature applications. A high phase fraction of intermetallic phases (e.g. y', y''), contributes to their high temperature durability, by precipitation strengthening. Polycrystalline Superalloys show a beneficial combination of high temperature durability, toughness and creep resistance. To predict the precipitation kinetics and microstructural evolution of these alloys simulation studies are executed. These simulations are carried out with the thermo-kinetic software package MatCalc. In the framework of this thesis simulation-models that describe important microstructural processes are presented and applied. For the verification of the simulation results, these are compared to literature and experimental data acquired within the Nenimov project.

Kurzfassung

Moderne Nickel-Basis-Superlegierungen sind komplexe, mehrphasige Materialien für Hochtemperaturanwendungen. Ein hoher Phasenanteil von intermetallischen Phasen (y', y'') trägt zu ihrer Hochtemperaturbeständigkeit, durch Ausscheidungsverfestigung bei. Polykristalline Superlegierungen weisen eine vorteilhafte Kombination aus Hochtemperaturbeständigkeit, Zähigkeit und Kriechfestigkeit auf. Um die Ausscheidungskinetik und Mikrostrukturentwicklung dieser Legierungen vorherzusagen, werden Simulationsstudien durchgeführt. Diese Simulationen werden mit dem thermokinetischen Softwarepaket MatCalc durchgeführt. Im Rahmen dieser Arbeit werden Simulations-Modelle zur Beschreibung wichtiger mikrostruktureller Prozesse vorgestellt und angewendet. Zur Verifizierung der Simulationsergebnisse werden diese mit Literatur und experimentellen Daten, die im Rahmen des Nenimov-Projekts gewonnen wurden, verglichen.

Acknowledgements

At first I would like to thank Prof. Kozeschnik and Dipl. Ing. Markus Rath for giving me the opportunity to expand my knowledge in the field of materials science and technology. They supported me in many different ways and the doors to their offices were always open for me whenever I had a question about my research or writing.

Financial support by the Austrian Federal Government (in particular from Bundesministerium für Verkehr, Innovation und Technologie and Bundesministerium für Wissenschaft, Forschung und Wirtschaft) represented by Österreichische Forschungsförderungsgesellschaft mbH and the Styrian and the Tyrolean Provincial Government, represented by Steirische Wirtschaftsförderungsgesellschaft mbH and Standortagentur Tirol, within the framework of the COMET Funding Programme is gratefully acknowledged.

Finally, I must express my very profound gratitude to my parents, my sister and Karina for providing me with unfailing support and continuous encouragement throughout my years of study and through the process of researching and writing this thesis. This accomplishment would not have been possible without them. Thank you.

Table of contents

Abstract II

Kurzfassung II

Acknowledgements III

Table of contents IV

1. Introduction 1

1.1. Background 1

1.2. Objectives 1

2. State of the art 3

2.1. Physical metallurgy of Nickel-base superalloys 3

2.1.1. Chemical composition and phases 3

2.1.2. Production process 6

2.1.3. Microstructure and mechanical properties 7

2.2. Microstructure evolution during thermo-mechanical processing 9

2.2.1. Plastic deformation 10

2.2.2. Microstructural mechanisms for substructure evolution 10

2.2.3. Microstructural mechanisms for grain structure evolution 11

2.3. Precipitation kinetic modelling 16

2.3.1. Basics of precipitation kinetics 16

2.3.2. Precipitation kinetic simulations with MatCalc 18

2.3.3. Thermodynamic models and CALPHAD approach 21

3. Modelling of microstructure evolution 23

3.1. Modelling of substructure evolution 23

3.1.1. Dislocation density evolution (ABC-model) 24

3.1.2. Work hardening 26

3.2. Modelling of grain-structure evolution 26

3.2.1. Recrystallization 26

3.2.2. Growth 28

4. Simulation and Results 32

4.1. Simulation setup 32

4.1.1. Thermo-kinetic system definition: Composition, phases and databases 32
4.1.2. Precipitation domain 33
4.1.3. Precipitate phases 34
4.1.4. Thermo-mechanical treatment 35
4.2. Part I: Precipitation kinetics simulation 36
4.2.1. Case study: Rene 65 36
4.2.2. Case study: IN-718 41
4.3. Part II: Simulation of microstructure evolution 43
4.3.1. Substructure evolution 43
4.3.2. Grain structure evolution 43
5. Discussion of results 51
5.1. Precipitation kinetics simulation 51
5.1.1. Preliminary study on Rene 88DT 51
5.1.2. Study on Rene 65 54
5.1.3. Study on Inconel 718 57
5.2. Microstructure evolution simulation 58
5.2.1. Work hardening and recovery 58
5.2.2. Dynamic recrystallization (DRX) 59
5.2.3. Meta-dynamic recrystallization (MDRX) 62
6. Summary and Conclusion 64
References 65
List of figures 68

1. Introduction

1.1. Background

Modern nickel-base superalloys are complex, multiphase materials for high temperature applications. They generally have a polycrystalline structure and show a beneficial combination of high temperature strength, toughness and creep resistance. The high temperature strength results from a high phase fraction of intermetallic phases (e.g. γ', γ''), that contribute to precipitation strengthening. When these alloys are processed, which is generally done by hot deformation, it is challenging to predict, their microstructural evolution. It is important to know how the microstructure behaves during thermomechanical treatments, to be able to control the processing conditions in a way that delivers a material with suitable properties. Especially the grain size is an important factor that has an impact on the properties of the final product. A way to predict the influence of thermomechanical treatments on material properties is computational engineering. This method combines theoretical models with empirical knowledge to provide solutions for a wide variety of challenges in the field of material development. The development of new high-performance alloys and the optimization of production processes can be achieved with advanced simulation software. Therefore, this way of material and process engineering is suitable to improve the properties of superalloys.

1.2. Objectives

This thesis deals with simulation studies, concerning precipitation kinetics and microstructure evolution during thermo-mechanical processing for different processing conditions. These investigations will also focus on the interaction of present secondary phases with microstructure evolution during thermo-mechanical treatments.

To increase the capabilities of present simulation software, research in the field of microstructure modelling and database development has to be done. To show which fields of research, concerning this topic, are the most promising or have to be improved for valid simulation results, simulation studies have to be performed. In the present thesis an approach to predict the microstructural evolution and precipitation kinetics of nickel base alloys, will be presented and discussed. The results that the applied models and databases deliver, will be evaluated based on two case studies for the alloys Rene 65 and Inconel 718.

The simulations in the present thesis are carried out with the thermo-kinetic software package MatCalc and the corresponding databases. In the framework of this thesis a chain of models to describe important microstructural processes is presented and applied. The goal of this

thesis is to verify that the microstructural evolution and precipitation kinetics of nickel based superalloys during processing, can be described by the models for substructure evolution and recrystallization that are currently implemented into MatCalc. The simulations should deliver results comparable to experimental results, from literature and data acquired within the Nenimov project. In particular the precipitation kinetics during heat treatments, strain hardening, and the recrystallization process during hot deformation will be considered in this thesis. This thesis includes two parts which include different tasks, which are summarized in the following:

Part I: Precipitation kinetics in Nickel-base superalloys

- Preliminary study to investigate the precipitation kinetic models and to identify the required model parameters.
- Precipitation kinetic study for two superalloys (Inconel 718 and Rene 65) to verify the simulation results with experimental data from literature and the Nenimov project.

Part II: Microstructure evolution in Nickel-base superalloys

- Preliminary study to investigate the different microstructural models (for plastic deformation, recovery, recrystallization, and grain growth) and to identify the required model parameters.
- Simulation study for the microstructure evolution of Inconel 718 superalloy with coupled precipitation kinetics and microstructural models to verify the simulation results with experimental data obtained within the Nenimov project.

2. State of the art

2.1. Physical metallurgy of Nickel-base superalloys

Nickel-base superalloys are highly alloyed materials, which contain around 50 % of nickel combined with different alloying elements. Nickel-base superalloys are generally used at temperatures above about 540 °C, and are used in a broad variety of high temperature application fields. Some examples are aerospace components, gas turbines, steam turbines, aircraft engines, components for chemical industry, etc. Therefore, this kind of alloys have to be resistant to mechanisms that would harm other alloys in their functionality at elevated temperatures.

2.1.1. Chemical composition and phases

This thesis will focus on two nickel base superalloys, namely Rene 65 (R-65) and Inconel 718 (IN-718). The nominal chemical composition of selected superalloys is given in Table 1.

Table 1: Nominal chemical composition for Inconel 718, Rene 65 and Rene 88DT

Alloy	Ni	Cr	Co	Mo	W	Fe	Al	Nb	Ti	Zr	C	B	N
IN-718	52.8	19	---	3	---	18.5	0.6	5.2	0.9	---	0.04	0.003	---
R-65	55.4	16	13	4	4	1	2.1	0.7	3.7	0.05	0.008	0.016	0.003
R-88DT	56.4	16	13	4	4	0	2.1	0.7	3.7	0.03	0.03	0.01	0.7

The alloying elements lead to different effects depending on the species of the added atoms. The impact, of commonly used alloying elements, on the properties of nickel-base superalloys, is shown in Table 2.

Ni-Matrix Phase

The crystal structure of nickel is generally face-centered cubic (fcc), this is one reason why nickel is used as basis for superalloys. The density of a superalloy is influenced by alloying additions, aluminum, titanium and chromium reduce density, whereas tungsten, rhenium and tantalum increase it. Corrosion resistance is determined mainly by the added alloying elements, particularly chromium and aluminium. The temperature limit for the usability of a nickel-base superalloys is determined by the incipient melting temperatures of alloys and solution temperatures of strengthening phases. Incipient melting means that some part of the alloy, when solidified, is not at equilibrium composition and therefore has a lower melting point than it would might have in equilibrium. Incipient melting temperatures and melting

ranges of alloys are functions of prior processing and composition. Even if there is no nonequilibrium segregation, alloys have rather a melting range than an exact melting point. The fcc matrices of superalloys possess excellent ductility, extended solubility for certain alloying additions and in the case of iron-nickel- and nickel-base superalloys favourable characteristics for precipitation of very effective strengthening phases [1].

Table 2: Role of alloying elements in superalloys [1]

Effect	**Alloying elements**
Solid-solution strengthening	Co, Cr, Fe, Mo, W,
Precipitation strengthening	Al, Ti, Nb
Oxidation resistance	Al, Cr,
Sulfidation resistance	Cr, Co, Si
Increases rupture strength	B(b)
Grain-boundary refiners	B, C

(a) Not all these effects necessarily occur in a given alloy. (b) If present in large amounts, borides are formed

Secondary phases

Not only the properties of the fcc matrix and its chemistry strengthens a superalloy but also the existence of strengthening phases, usually precipitates. Mechanical treatments like working (mechanical deformation, often cold) are also able to increase the strength of a superalloy, but the effect responsible for this kind of strengthening may not withstand high temperatures. Table 3 shows important precipitates that occur in nickel base superalloys, and their properties. While in the Inconel 718 alloy y', y'', and delta precipitates are observed, the Rene 65 generally only contains y' particles in an amount that is noteworthy. For the properties of these secondary phases see Table 3.

Table 3: Properties of precipitation phases that occur in Rene-65 or IN-718 [1]

Phase	***Crystal structure***	***Lattice parameter [nm]***	***Formula***	***Comments***
γ'	*Fcc* *(ordered L12)*	*Ni_3Al:* *$a_0 = 0.3561$* *$Ni_3(Al_{0.5}Ti_{0.5})$:*	*$Ni_3(Al, Ti)$*	*Principal strengthening phase in many nickel- and nickel-iron-base superalloys; crystal lattice varies slightly in size (0 to 0.5%) from that of austenite matrix; shape varies from spherical to cubic; size varies with exposure time and temperature. Gamma-prime is spherical in iron-nickel-base and in some of*

		a_0 = 0.3568		*the older nickel-base alloys, such as Nimonic 80A and Waspaloy. In the more recently developed nickel-base alloys, γ‘ is generally cuboidal. Experiments have shown that variations in molybdenum content and in the aluminum/titanium ratio can change the morphology of γ‘. With increasing γ/γ‘ mismatch, the shape changes in the following order: spherical, globular, blocky, cuboidal. When the γ/γ‘ lattice mismatch is high, extended exposure above 700 °C causes undesirable η (Ni_3Ti) or δ (Ni3Nb) phases to form.*
γ‘‘	*bct* *(ordered DO_{22})*	a_0 = 0.3624 c_0 = 0.7406	Ni_3Nb	*Principal strengthening phase in Inconel 718; γ‘‘ precipitates are coherent disk-shaped particles that form on the {100} planes (average diameter approximately 600 Å, thickness approximately 50 to 90 Å). Bright-field transmission electron microscopy (TEM) examination is unsatisfactory for resolving γ‘‘ due to the high density of the precipitates and the strong contrast from the coherency strain field around the precipitates. However, dark-field TEM examination provides excellent imaging of the γ‘‘ by selective imaging of precipitates that produce specific superlattice reflections. In addition, γ‘‘ can be separated from γ‘ using the dark-field mode, because the γ‘‘ dark-field image is substantially brighter than that of γ‘.*
δ	*Orthorhombic* *(ordered Cu_3Ti)*	a_0 = 0.5106–0.511 b_0 = 0.421–0.4251 c_0 = 0.452–0.4556	Ni_3Nb	*Observed in overaged Inconel 718; has an acicular shape when formed between 815 and 980 °C; forms by cellular reaction at low aging temperatures and by intragranular precipitation at high aging temperatures*

In addition to these phases carbides, nitrides and brittle topologically close packed (TCP) phases can occur. The elements that lead to their formation are shown in Table 4.

Table 4: Elements for phase formation

Carbide formers:	
MC	W, Ti, Mo, Nb
M_7C_3	Cr
$M_{23}C_6$	Cr, Mo, W
M_6C	Mo, W, Nb
Carbonitrides: M(CN)	C, N

2.1.2. Production process

Nickel-base superalloys are produced in different ways. Some methods that can be used for the alloys Inconel 718 and Rene 65 rare described in this chapter. For a more detailed review on this topic see the references Donachie et al. [1] and Dieter et al. [2]. Figure 1 shows different production methods for nickel-base superalloys.

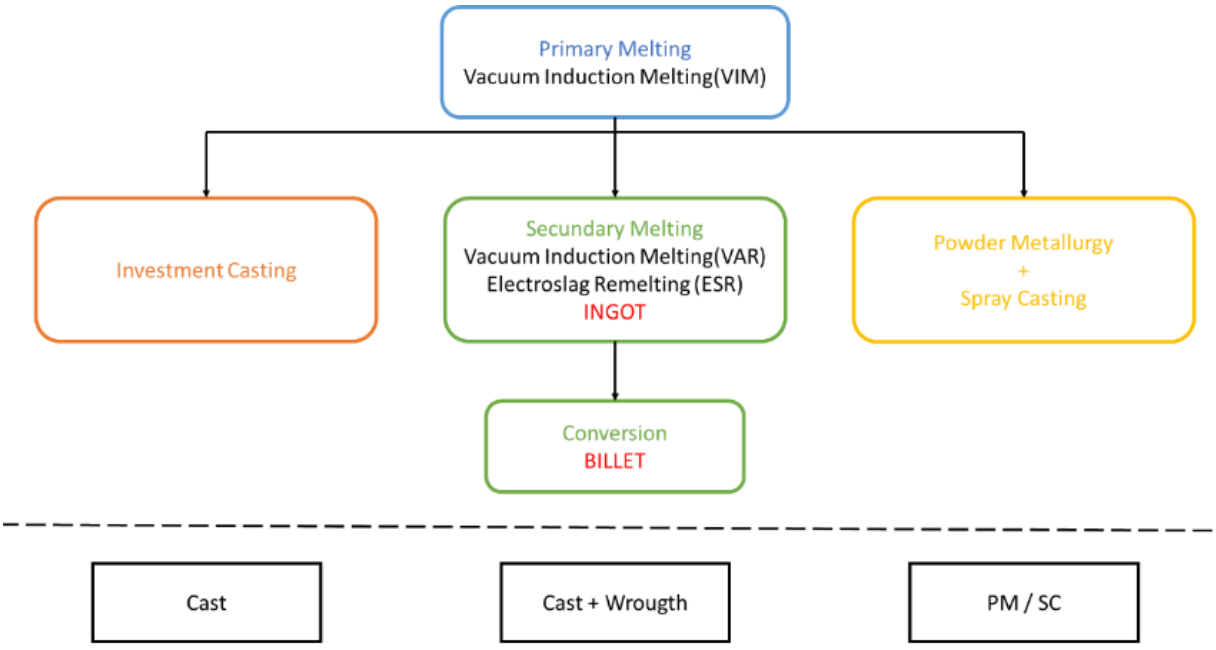

Figure 1: Production routes for nickel-base superalloys.

The alloy Rene 88DT (R-88DT) is produced by the powder metallurgy route, while the Inconel 718 (IN-718) can be processed by investment casting or by the cast and wrought method, whereas the cast and wrought route is the most common one. This route includes two processing steps, melting and ingot conversion. An alloy that has similar composition to R-88DT but can be produced by the cast and wrought route is Rene 65 (R-65). Since the IN-718 and the Rene 65 alloy can be produced via the cast and wrought route, a more detailed description for this method is given in the following.

Casting (triple melting)

In a primary melting step the vacuum induction melting (VIM) process is used to obtain an initial electrode with low oxygen and precise chemistry, which is followed by a second refining step, the electroslag remelting (ESR). As a result, the ESR electrode will be clean and sound but may contain freckles. To obtain the final segregation-free structure a third melting process, vacuum arc remelting (VAR) process, is applied.

Ingot Conversion

To produce mill products out of the ingot obtained after the melting process, hot working operations are applied. Mill products are separated into two classes: long products (billets and bars) and flat products (plates and sheets). To reduce compositional gradients created in the ingot it is possible to simply expose the ingot to high temperatures during hot deformation. For more complex compositions a homogenization step is often needed. The major operations used for ingot breakdown are cogging (forging), rolling, or extrusion. Superalloys are process-history sensitive, therefore thermo-mechanical processing cycles can have an important effect on the properties of the final product.

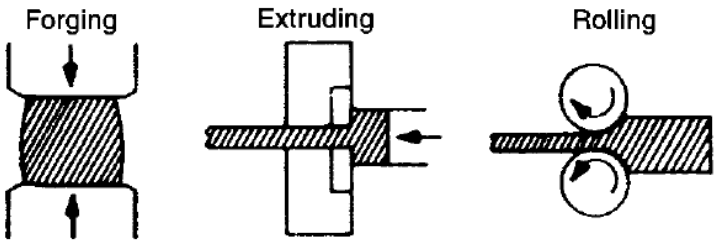

Figure 2 Schematic illustration of major operations used for ingot breakdown [1]

2.1.3. Microstructure and mechanical properties

Microstructure of the billet material

The microstructure of the as received material of the two investigated alloys is shown in Figure 3. Both alloys have a polycrystalline structure. At the grain boundaries of the Inconel 718, delta precipitates can be found. The y' and y'' particles, which are present in the Inconel 718 are not directly seen due to their small size, but they cause the dark shades within the grains. The Rene 65 alloy contains only y' precipitates. The primary y' precipitates are the small spheres that are spread in the matrix in the micrograph. Similar to the Inconel 718 the smaller secondary y' precipitates are not directly seen.

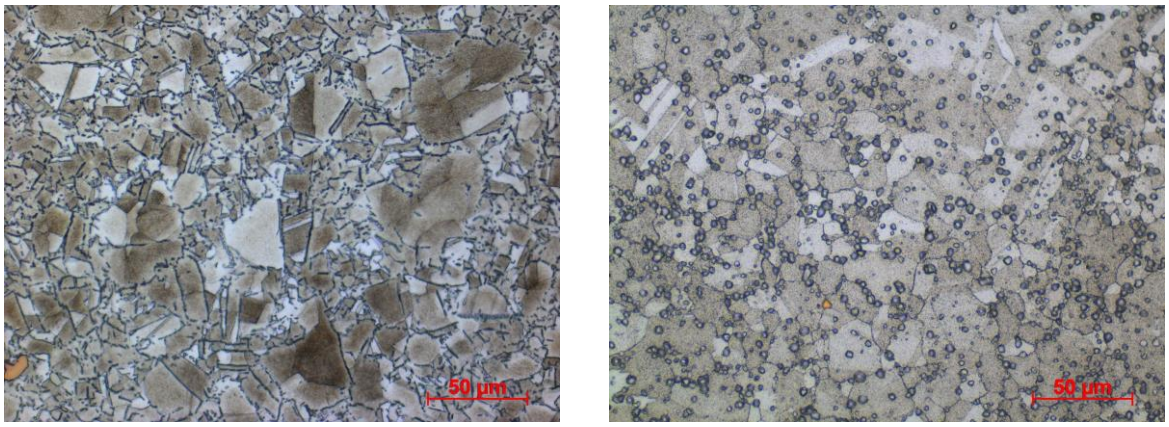

(a) Inconel 718 (b) Rene 65

Figure 3: microscope images of as received material; polished and etched.

The strengths of metals are commonly measured in terms of short time properties such as yield strength or ultimate strength. But at elevated temperatures, e.g. about 50 % of the melting point/range, strengths have to be reckoned time depended. If a metal is subjected to stress considerably less than the amount of stress that would break it at room temperature, but if it is at high temperature, it will begin to deform over time. This time dependent extension is called creep. If this process continues for a certain time, it will lead to fracture or rupture. Therefore, the creep and rupture strengths of a metal are necessary to understand its mechanical properties, just as much as are the yield strength and ultimate strengths. The fatigue (cyclic) capability will be reduced in a similar way. Thus, to validate the properties of an alloy, dependent on application temperature and load, it is important to provide yield and ultimate strengths, creep strengths, stress-rupture strengths, and appropriate fatigue strengths. Other mechanical properties such as crack growth rates, dynamic modulus, and fracture toughness and physical properties as thermal expansion coefficient, density, etc. also may be required. Different methods to achieve desirable properties for a superalloy, are schematically described in the following.

Strengthening mechanisms

To achieve appropriate mechanical properties at high temperatures the following hardening mechanisms can be used.

a) Solid Solution strengthening: Alloying elements are added to the base material in order to increase strength. This effect is based on stress that is induced into the crystal lattice due to the size difference between the matrix element and the additional elements and the bonds formed between them.

$$\Delta\sigma_S = \alpha G c^{1/2} \qquad (1)$$

In equation (1), α gives the specific strengthening effect of an atom, c is the concentration of the added element and G is the shear modulus.

b) Fine grain (Hall-Petch) strengthening: This method is based on the effect that a material with smaller grains has an increased strength compared to an otherwise identical material with bigger grains. Finer grains often lead to higher strengths without loss in toughness. However, this method is not always suitable for high temperature applications because smaller grains also mean more grain boundaries which act as diffusion paths. Thus, smaller grains mean faster diffusion which favours undesirable high temperature effects like creep.

$$\Delta\sigma_{\mathrm{FG}} = kS^{1/2} \quad (2)$$

In equation (2), S is the grain diameter and k is a material parameter.

c) Particle strengthening: The existence of particles in the matrix can lead to higher strength. This increase in strength is a result of these particles being obstacles for the movement of dislocations and grain boundaries. The more and finer dispersed these particles are, the stronger is this effect generally.

$$\Delta\sigma_{\mathrm{P}} = \alpha GbS^{-1} = \alpha Gbf^{1/2}d^{-1} \quad (3)$$

In equation (3), α is a scaling parameter, b is the burgers vector, S is the average distance between the particles, *f* is the particles volume fraction, and *d* is the diameter of the particles.

2.2. Microstructure evolution during thermo-mechanical processing

Nickel-base superalloys are often deformed in the manufacturing process. When deformation, e.g. strain is introduced into a metallic material, two competing microstructural mechanisms can occur. These mechanisms are recovery and recrystallization, and are illustrated in Figure 4. The recovery rate in nickel base alloys is generally very low, due to the low stacking fault energy in these alloys. Therefore, the dynamic recrystallization process is more likely to occur and plays an important role for the processing of nickel-base superalloys [3].

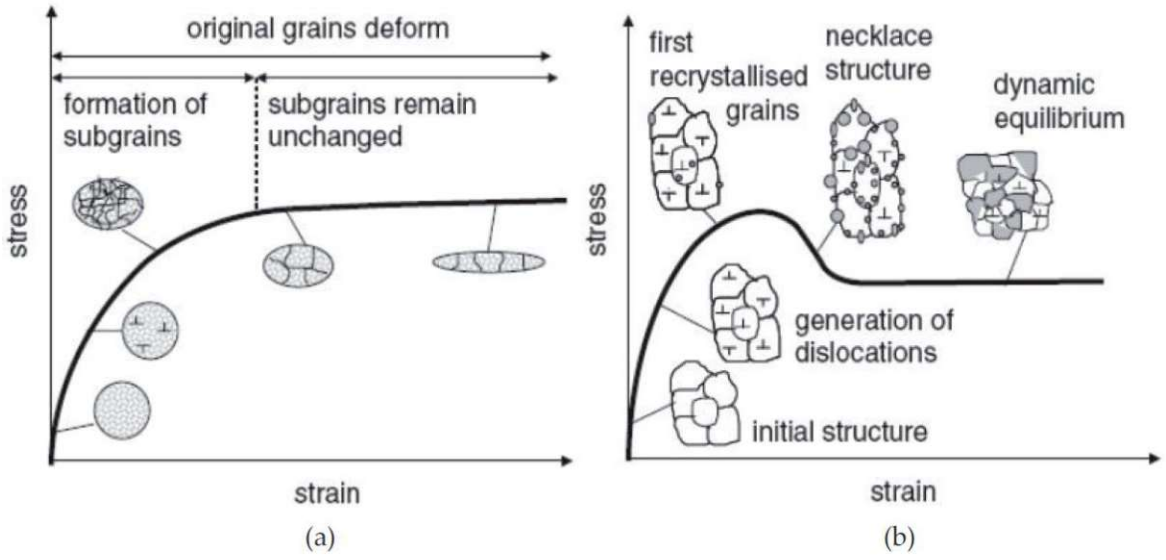

Figure 4: Effect of microstructural mechanisms on the flow curve (a) recovery, and (b) recrystallization. [3]

2.2.1. Plastic deformation

Plastic deformation of a metal is linked to the movement of dislocations within the lattice structure. Dislocations move along certain glide-planes which are determined by the type of lattice structure of the material. Some of these glide-planes are not active at room temperature but only at elevated temperatures. Plastic deformation can also be possible due to the formation of so called deformation twins. Twins occur when two crystal lattices share some lattice points. For more information about twinning see Christian and Mahajan [4]. The models used in this thesis focus on dislocation movement and neglect twinning in the description of plastic deformation [5].

2.2.2. Microstructural mechanisms for substructure evolution

Microstructural mechanisms that govern the substructure evolution of metallic materials are summarized in this section.

Strain hardening

Strain or work hardening describes the effect that plastic deformation leads to higher strength values. This happens because dislocations are produced during deformation, for example in so called frank read sources. The dislocations hinder the movement of each other because they form kinks and jogs. Therefore the strength of a material increases with the number of dislocations generated during deformation [5].

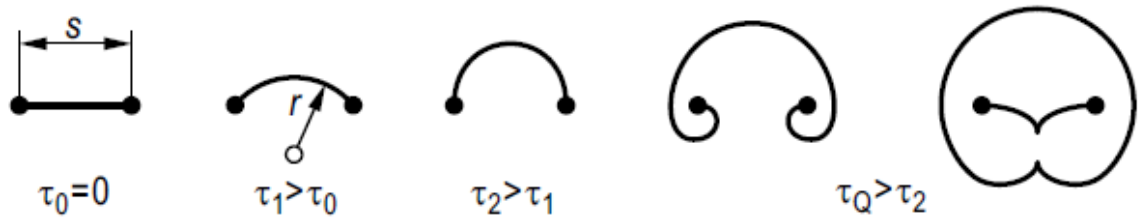

Figure 5: A dislocation that is pinned at two points (for example at precipitates) becomes a "frank read source" at a certain stress level (τ_Q). [5]

Recovery

All defects in a metal that are not in thermodynamic equilibrium show a tendency to "heal". This means that for example two dislocations meet and annihilate each other, if their burgers vectors are of opposite sign. This process starts, as the defects are able to move which means at temperatures above 0 K. How fast the recovery process works, is mainly determined by the type of defect, activation energy for defect movement, temperature and defect concentration.

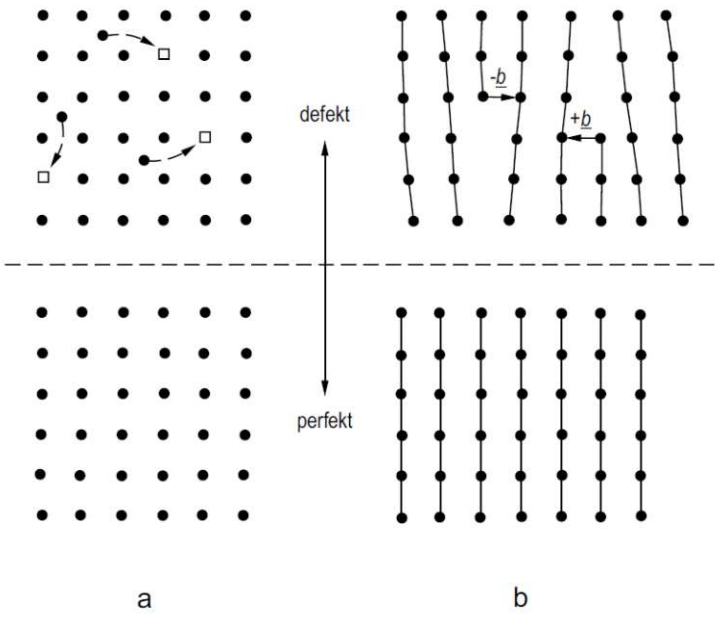

Figure 6: Recovery of defects (annihilation), a: interstitial atom reacts with vacancy; b: line dislocations with opposite burgers vector directions react with each other. [5]

There exist other recovery mechanisms where defects do not vanish but just change their identity. For example: condensation of vacancies, rearrangement of dislocations with the same burgers vector direction, which leads to the formation of low angle grain boundaries [LAGB], condensation of many dislocations that results in formation of high angle grain boundaries [HAGB]. These are shown in Figure 7.

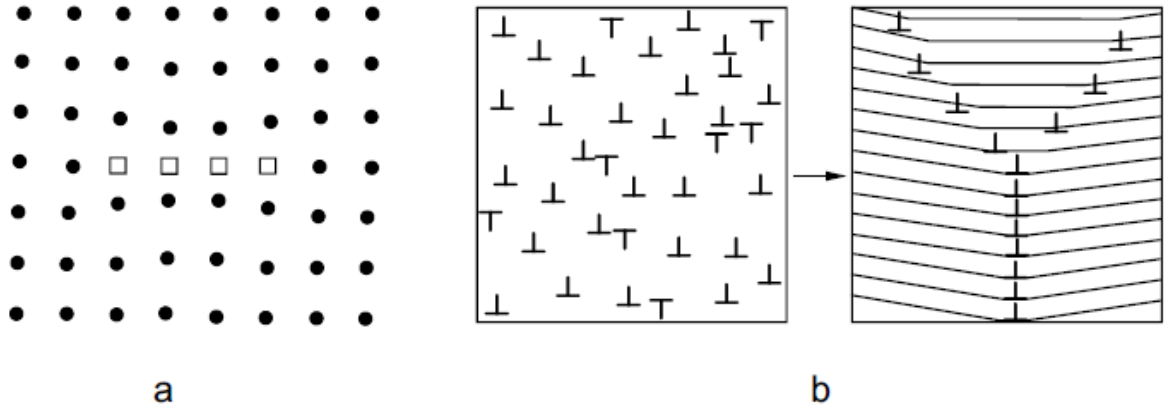

Figure 7: Rearrangement of defects. A: vacancies form "dislocation-ring"; b: Dislocations annihilate and form LAGB. [5]

2.2.3. Microstructural mechanisms for grain structure evolution

The evolution of the grain structure in nickel-base superalloys is mainly governed by recrystallization and grain growth. The type of recrystallization that is most important for this

group of alloys will be specified and basic concepts behind the description of both mechanisms will be described in this section.

Recrystallization

Different types of recrystallization are known, namely static recrystallization (SRX), dynamic recrystallization (DRX), and meta-dynamic recrystallization (MDRX). When cold deformation is performed, and the material is heated afterwards, SRX occurs. DRX is a process where recrystallization takes place during deformation at elevated temperatures. If the recrystallization process is still active after DRX one speaks of MDRX. Different types of DRX are distinguished. The discontinuous DRX (DDRX) process consist of two stages, nucleation and growth while the continuous DRX (CDRX) is characterized by progressive transformation. Figure 8 illustrates the different types of DRX. [6]

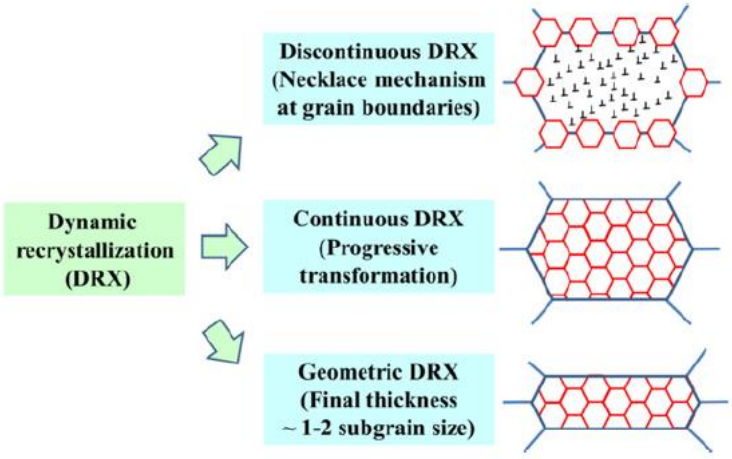

Figure 8: Different types of DRX [6]

Discontinuous dynamic recrystallization (DDRX)

The formation of new HAGB in a deformed metal is called recrystallization, because new defect free grains are produced through this process. With increasing deformation there is an increasing number of areas with dislocation structures similar to grain boundaries. If these areas are able to move they act as nuclei for recrystallization. They move due to an energy difference between a crystal with defects and a defect-free crystal. The force resulting from this energy difference is defined as change of the free enthalpy per unit volume of the area passed by the moving grain boundary (p_R). This correlation can be expressed by equation (4):

$$p_R = -\frac{dG}{dV} = -\frac{1}{A}\frac{dG}{dx} \sim \rho_H - \rho_N \qquad (4)$$

where ρ_H is the dislocation density before and ρ_N is the dislocation density after recrystallization [5]. The mechanism that is used as base for the model that describes the recrystallization evolution in this thesis, is the so called Bailey Hirsch mechanism [7]. According to this approach a portion of a more perfect grain might migrate into a less perfect grain if a difference in dislocation density exits between these two grains. The driving force for this process is associated with the strain energy difference across the boundary. This migration is accomplished by the forward movement of the grain boundary to form a bulge, as shown in Figure 9. The moving boundary sweeps up the dislocations in its path and thereby creates a small, relatively strain-free volume of crystal. When this bulge exceeds the critical nucleus size, both primary conditions for the formation of a nucleus are satisfied [8].

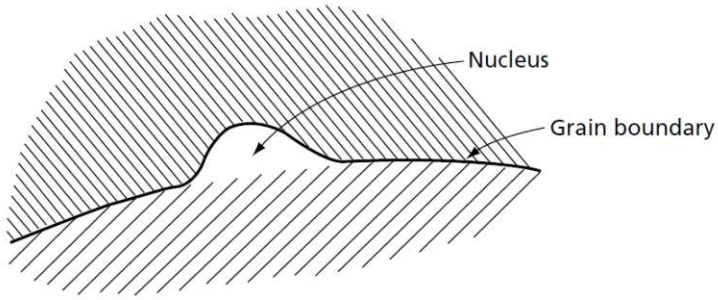

Figure 9: The bulge mechanism for the formation of a nucleus at a grain boundary. [8]

The critical nucleus size for recrystallization is depending on surface and volume energy, and can be summarized with equations (5) - (8).

$$E_{\text{Surface}} = 4\pi r^2 \gamma_{\text{HB}} \tag{5}$$

$$\frac{\partial E_{\text{Surface}}}{\partial r} = 8\pi r \gamma_{\text{HB}} \tag{6}$$

$$\frac{\partial E_{\text{Volume}}}{\partial r} = 4\pi r^2 P_{\text{D}} \tag{7}$$

Nucleation will occur spontaneously if:

$$\frac{\partial E_{\text{Volume}}}{\partial r} > \frac{\partial E_{\text{Surface}}}{\partial r} \rightarrow r_{\text{crit}} = \frac{2\gamma_{\text{HB}}}{P_{\text{D}}} \tag{8}$$

Here γ_{HB} is the surface energy of high angle grain boundaries and P_{D} is the driving force for growth.

Effect of processing parameters on DDRX

A variety of processing parameters have an impact on the DDRX. The influence of temperature, strain rate and initial grain diameter on flow stress, recrystallization and grain size evolution is described in this section.

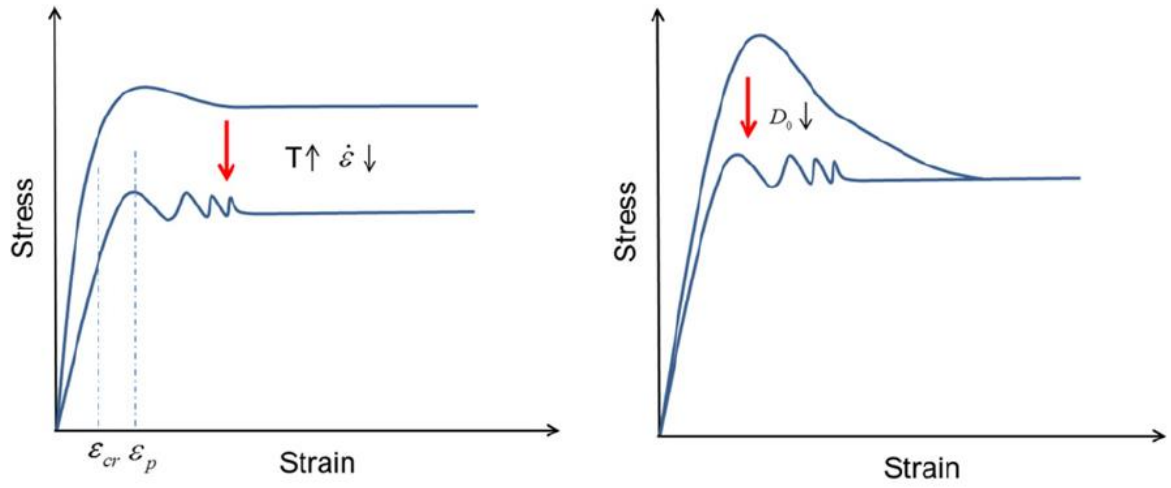

a) Effect of temperature and strain rate b) Effect of initial grain size

Figure 10: Effect of processing parameters on flow stress. [6]

The flow stress decreases when temperature is increased, or the strain rate is decreased. A lower initial grain size leads to an initially higher flow stress. The evolution of recrystallized volume fraction is also strongly dependent on the initial grain size and the processing parameters as seen in Figure 11.

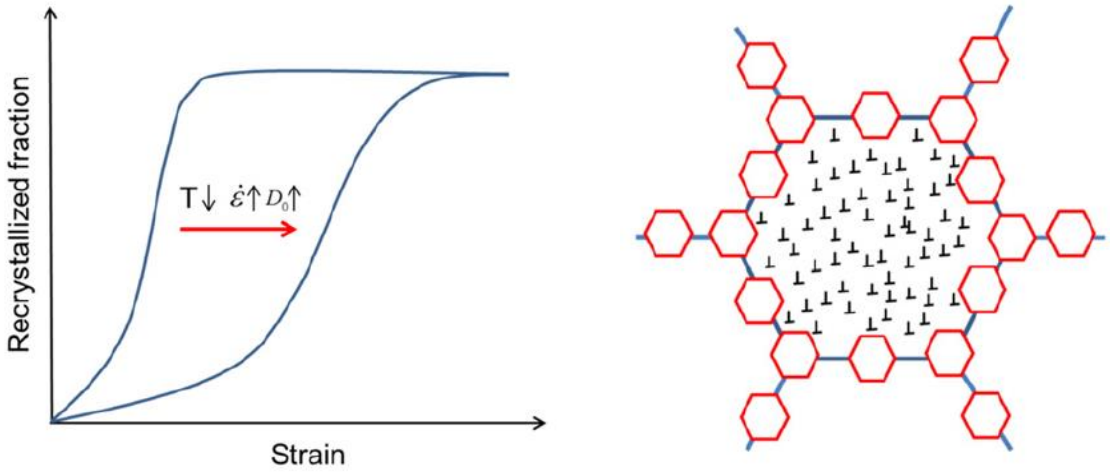

a) Effect of temperature, strain rate and initial grain diameter.

b) grain boundaries serve as nucleation sites

Figure 11: Effect of processing parameters on recrystallized volume fraction. [6]

The recrystallization is postponed to higher strain levels for a higher initial grain size or when the temperature is decreased, or the strain rate is increased.

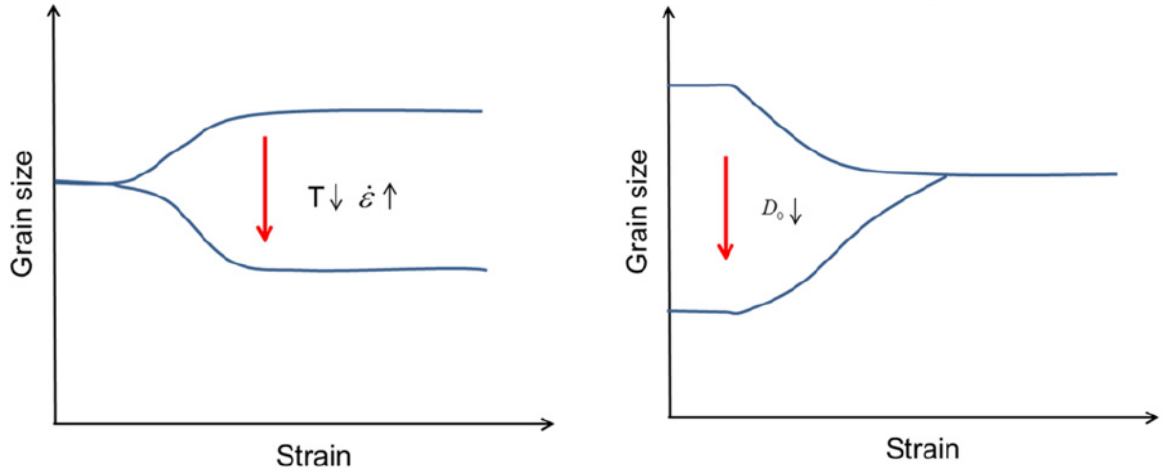

a) Effect of processing parameters

b) Effect of initial grain size

Figure 12: Effect of processing parameters on grain size evolution. [6]

Independently on the initial mean grain size, the steady state grain size after dynamic recrystallization is dependent on the processing parameters (e.g. temperature and strain rate) as shown in Figure 12 (a). Additionally, as it can be seen in Figure 12 (b), the initial mean grain size is always evolving to the steady state grain size during dynamic recrystallization.

Grain growth

There are generally two kinds of grain growth, normal grain growth and abnormal grain growth. During normal grain growth, the size distribution of the grains stays relatively uniform.

Abnormal grain growth describes the process of some grains growing rapidly at the cost of the other grains. The theory of normal grain growth is based on the principle of grain boundary free energy, which is the driving force for this process. Abnormal grain growth normally occurs when normal growth cannot take place due to the presence of second phase particles and when there is at least one grain that is much larger than the average. The models used for simulations in the present thesis only take normal grain growth into account. A more detailed review of this topic is given by Hillert [9].

2.3. Precipitation kinetic modelling

This chapter should give some insight on how precipitates are dealt with in the framework of simulations. Therefore, some basic information about precipitation is given in the first part. The second part of this section schematically describes how precipitation kinetic simulations are treated in MatCalc. At the end of this section a short summary is given, concerning the databases in MatCalc which are based on the Calphad approach.

2.3.1. Basics of precipitation kinetics

Precipitation is a process in which a new phase is created within the volume of a so-called parent phase. At the beginning, these new precipitates are relatively small compared to the volume of the parent phase and appear in high number densities. The precipitates differ from the parent phase by chemical composition, crystal structure, local ordering and other properties. The evolution of precipitates is commonly described within three stages: nucleation, growth and coarsening. It has to be considered that these stages are not sharply distinguished but can occur overlapped in a temporal sequence.

Nucleation

The first step in the evolution of precipitates is nucleation. This is considered as a stochastic process and has to be handled in a statistical framework, because it is not possible to predict, if a single nucleation event at a specific position will occur or not. However, it is possible to give a more or less correct probability that a certain number of nucleation events take place within a specified volume. In the context of precipitates that form in a solid matrix the term Solid-State Nucleation is used to distinguish it from other nucleation processes like the formation of droplets in supersaturated vapour. Although these two mechanisms are different in some ways, the quantitative theory of solid-state nucleation can be widely based on the relations derived for droplet formation. Due to its complexity the process of nucleation is just described schematically in the framework of this thesis. Here, only the equations for the free energy of the nuclei, ΔG_{nucl}, the critical nucleation radius, r^*, the critical nucleation energy, G^*, and the steady-state nucleation rate, J_{s}, are mentioned. These equations are placed here so that one can see the relationship between the nucleation rate and the governing Parameter, G^*.

$$\Delta G_{\mathrm{nucl}} = \frac{4}{3}\pi\rho^3.\Delta G_{\mathrm{vol}} + 4\pi\rho^2.\Delta G_{\mathrm{surf}} \tag{9}$$

$$r^* = -\frac{2\Delta G_{\mathrm{surf}}}{\Delta G_{\mathrm{vol}}} \tag{10}$$

$$G^* = \frac{16\pi}{3}\frac{(\Delta G_{\mathrm{surf}})^3}{(\Delta G_{\mathrm{vol}})^2} \tag{11}$$

$$J_{\mathrm{s}} = NZ\beta^* \exp\left(-\frac{G^*}{k_{\mathrm{b}}T}\right) \tag{12}$$

In these equations N is the number of potential nucleation sites, Z is the Zeldovich factor, β^* is the atomic attachment rate, k_{b} is the Boltzmann constant, and T is the absolute temperature. Furthermore, there are many effects to consider which are important for the evolution of precipitates like the volume misfit stress, heterogeneous nucleation mechanics, nucleation site saturation, etc. In addition, there is a variety of models implemented into MatCalc, which use different assumptions on how to calculate the nucleus composition .For detailed information on these topics see Kozeschnik et al. [10].

Growth

While the nucleation phase is stochastic in nature, the laws that control the growth process of precipitates are deterministic and can be described by appropriate evolution equations. Generally, the growth of secondary phases is considered as a diffusion controlled process. The precipitates grow due to a continuous stream of precipitate forming atoms which attach to the surface of precipitates. This kinetic process is governed by diffusional fluxes, J_i, of components i in the matrix phase and in the precipitate. Figure *13* shows the composition profile for a B-rich precipitate that grows in an A-rich matrix. The concentration gradient at the interface induces diffusional fluxes, J, given by Fick's first law as

$$J_B^{\alpha} = -D_{\mathrm{B}}^{\alpha}\frac{\partial c_{\mathrm{B}}^{\alpha}}{\partial r} \tag{13}$$

$$J_{\mathrm{B}}^{\beta} = -D_{\mathrm{B}}^{\beta} \frac{\partial c_{\mathrm{B}}^{\beta}}{\partial r} \tag{14}$$

with D_{B}^{α} being the diffusion coefficient of element B in phase α, r being the spherical radius coordinate and c_{B}^{α} being the concentration.

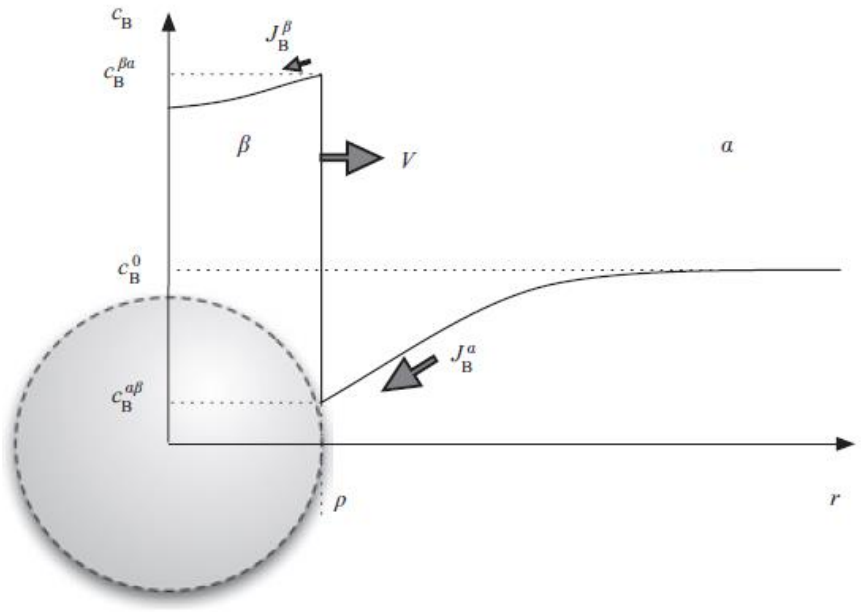

Figure 13: Schematic representation of a B-rich spherical precipitate growing in a supersaturated matrix. [10]

Coarsening

Ostwald ripening, also known as coarsening, describes the effect that larger and therefore thermodynamically more stable particles grow at the expense of smaller particles. The driving force for coarsening is the minimization of the total interfacial energy by reducing the interface area. A mathematical description and further information is given by Kozeschnik et al. [10].

2.3.2. Precipitation kinetic simulations with MatCalc

The simulations in this thesis are performed with the thermo-kinetic software package MatCalc and the related thermodynamic and kinetic databases. The employed version of MatCalc was 6.00.1000, in combination with the corresponding nickel databases. The following explanations and descriptions are based on the book of Kozeschnik et al. [10], which is also a good source for further information concerning this topic.

Basics concepts of MatCalc

Precipitation kinetic simulations in MatCalc are based on the thermodynamic principle of maximum entropy production and the mean-field representation of the precipitation problem. These two approaches make it possible to describe the evolution of radius and chemical composition of each precipitate, with a linear system of equations. Therefore, even complex problems, concerning precipitation, can be simulated in a computationally efficient way. Another important model in MatCalc is the nearest-neighbour broken-bond model that allows the determination of interfacial energies based on an effective structural factor and the enthalpy of solution. To describe the evolution of precipitates, evolution equations are derived from the thermodynamic extremal principle in the framework of the mentioned mean-field approach. In MatCalc, the Kampmann-Wagner approach is used to perform the time integration of these evolution equations.

Kampmann-Wagner approach

In the framework of this approach the precipitation distribution is treated in terms of discrete size classes for precipitates of identical radius and chemical composition. For the process of time integration, the entire simulation schedule is discretized into sufficiently small isothermal time increments. At the start of a time step, the nucleation rate equation is evaluated for each precipitate that is assigned to the precipitation reaction. If applicable new size classes are added to the existing ones, based on the results of the nucleation rate equations. Afterwards the growth equations are evaluated for all existing size classes and radius and chemical composition of the size classes are updated. When the radius of a particular size class falls below a certain threshold value, the concerned size class is removed. If the maximum number of size classes is reached and new classes should be created according to the nucleation rate equation MatCalc rearranges the size class distribution to match the maximum settings. Figure 14 schematically illustrates the calculation process in MatCalc during precipitation kinetic simulations.

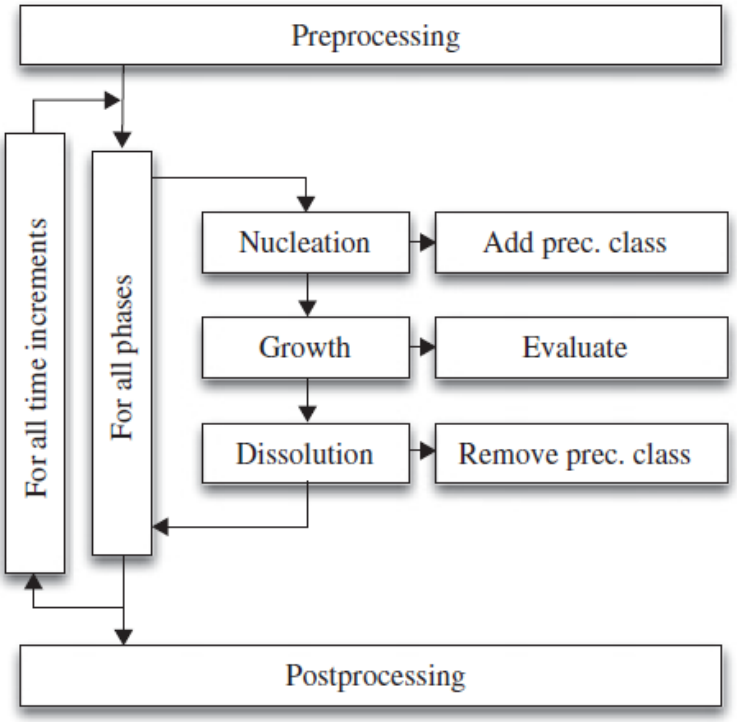

Figure 14: Time integration of the evolution equations as implemented in MatCalc. [10]

Diffuse interfacial energy correction (Tcrit)

To describe diffuse interfaces in MatCalc a diffuse interfacial energy correction term was added to the interface energy models. The model for precipitate interfaces in MatCalc is based on the so called Generalized Broken-Bond (GBB) model, which was developed by Sonderegger and Kozeschnik [11] on the basis of the Nearest-Neighbour Broken-Bond (NNBB) approach of Becker [12] and Turnbull [13]. To be able to describe diffuse interfaces, a diffuse interface correction factor, $\beta(K)$, was introduced by Sonderegger and Kozeschnik [14]. This factor is dependent on the regular solution critical temperature, T_{C}, which is the highest possible solution temperature, for a two-component system, with the composition $x_A = x_B = 0.5$. T_{C} is defined as

$$T_C = \frac{\Delta H_{\mathrm{sol,0K}}}{2R} \tag{15}$$

with $\Delta H_{\mathrm{sol,0K}}$ being the solution enthalpy at 0 K and R being the gas constant. The correlation between, $\beta(K)$, and T_{C} is given by

$$K = \frac{T}{T_{\mathrm{C}}} \tag{16}$$

and

$$\beta(K) = \begin{cases} 8.4729K^6 - 26.691K^5 + 32.717K^4 \\ -17.674K^3 + 2.2673K^2 \\ -0.09K + 1.00047632 \\ 1 \end{cases} \begin{matrix} \\ \\ \\ \end{matrix} \begin{matrix} , for\ K\ > 0.07 \\ \\ \\ , otherwise \end{matrix} \quad (17)$$

Finally, one gets the diffuse interface energy through equation (18):

$$\gamma_{\mathrm{GBB,diff}} = \gamma_{\mathrm{GBB,sharp}}\beta(K) \quad (18)$$

2.3.3. Thermodynamic models and CALPHAD approach

Thermodynamic calculations in MatCalc are based on the Calphad approach.[15] This approach will be explained based on Wu et al. [16]. It is assumed that the location of a phase boundary is the result of stability competition between two or more phases. Calphad databases are developed using a phenomenological approach. In a first step thermodynamic models for all constituent binary systems are derived. The selected model type should correspond with the physical and thermodynamic properties of the concerned phase. Common phases in in Ni-base superalloys are the γ phase (a disordered solid solution), and ordered intermetallic phases like, γ', γ'' and δ phase. Disordered solution phases are described by a substitutional type model. [17] The Gibbs energy of this kind of phase in a binary system can be expressed by:

$$G_{\mathrm{m}}^{\Phi} = \sum_{i=\mathrm{A,B}} x_i G_i^{\Phi,0} + RT \sum_{i=\mathrm{A,B}} x_i\, lnx_i + \sum_{v} L_v\,(x_{\mathrm{A}} - x_{\mathrm{B}})^v \quad (19)$$

The first term on the right-hand side of the equation represents the reference state, with x_i being the mole fraction of component i, and $G_i^{\Phi,0}$ the Gibbs energy of pure component i with Φ structure. The second term is the ideal mixing term and the last one is the excess Gibbs energy of mixing, with L_v being the interaction coefficient, and v the power of polynomial series. Different values for v are used for different solution models. When v = 0, it is a regular solution model, otherwise if v is between 0 and 1, it is a sub-regular solution model, and so on. Generally, these model parameters are optimized to fit best to the available experimental data.

Ordered intermetallic phases are described by different sublattice models, for example the compound energy model and the bond energy model. These models describe the Gibbs energy as a function of the sublattice species concentrations and temperature. The Gibbs energy of a binary intermetallic phase described by a two-sublattice compound energy model, $(A,B)_{\mathrm{p}}:(A,B)_{\mathrm{q}}$, can be written as:

$$
\begin{aligned}
G_{\mathrm{m}}^{\Phi} = & \sum_{i=\mathrm{A,B}} \sum_{j=\mathrm{A,B}} y_i^I y_j^{II} G_{i:j}^{\Phi} \\
& + RT \left(\frac{p}{p+q} \sum_{i=\mathrm{A,B}} y_i^I \ln y_i^I + \frac{p}{p+q} \sum_{i=\mathrm{A,B}} y_i^{II} \ln y_i^{II} \right) \\
& + \sum_{j=\mathrm{A,B}} y_{\mathrm{A}}^I y_{\mathrm{B}}^I y_j^{II} \, (y_{\mathrm{A}}^I - y_{\mathrm{B}}^I)^v L_{\mathrm{A,B}:j}^v \\
& + \sum_{j=\mathrm{A,B}} y_i^I y_{\mathrm{A}}^{II} y_{\mathrm{B}}^{II} \, (y_{\mathrm{A}}^{II} - y_{\mathrm{B}}^{II})^v L_{i:\mathrm{A,B}}^v + y_{\mathrm{A}}^I y_{\mathrm{B}}^I y_{\mathrm{A}}^{II} y_{\mathrm{B}}^{II} L_{\mathrm{A,B:A,B}}
\end{aligned}
\tag{20}
$$

Where y_i^I and y_i^{II} are the species concentrations of component i in the first and second sublattice, respectively. On the right-hand side, the first term is the reference state with the mechanical mixture of pure compounds: $A, A_{\mathrm{p}}B_{\mathrm{q}}, B_{\mathrm{p}}A_{\mathrm{q}}$, and B. $G_{i:j}^{\Phi}$ represents the Gibbs energy of the stoichiometric compound $i_p j_q$ with Φ structure. If $i_{\mathrm{p}}j_{\mathrm{q}}$ is a stable compound, the value of $G_{i:j}^{\Phi}$ can be obtained experimentally. Otherwise it is either a model parameter obtained by optimization using experimental data related to this phase or it can be obtained with "ab inito" calculations.

When thermodynamic descriptions for all constituent binaries are established, preliminary descriptions for the ternaries can be obtained by extrapolation of the binary model parameters. Therefore geometric models, such as the Muggianu model [18] are used. Ternary interaction model parameters are applied to improve the description of ternary systems when reliable experimental data is available. High-order systems are approached with the same strategy.

3. Modelling of microstructure evolution

To describe microstructural evolution processes in a numerical way that is suitable for simulations, in the framework of the software package MatCalc, different model variations are available. There exist different approaches for grain growth, work hardening etc. For simulations done within this thesis a so called “single class model” for the evolution of the mean grain size was applied, due to its stability and good compatibility with the model for recrystallization. Approaches that are necessary to describe dislocation density evolution and recrystallization will be summarized in the following sections.

3.1. Modelling of substructure evolution

The substructure of an alloy is strongly depended on the density of dislocations. This characterising value is therefore taken as a state parameter to describe the substructure evolution. The dislocation density, ρ, influences the size evolution of subgrains, which in turn influences recrystallization behaviour in the applied model. Due to this relationship, the dislocation density has a high impact on the outcome of the simulations that are carried out within this thesis. Plastic deformation, which influences the dislocation density, can be described in the framework of four stages. Stage 1 is defined by easy glide, where only one slip system is active and only pre-existing obstacles are restricting barriers for dislocation motion. When additional slip planes are activated by further deformation, dislocations on intersecting slip planes start to interact. At this point stage 2 starts, which is characterized by a linear strengthening rate. Stage 3 begins when the flow curve deviates from linearity. This is caused by dynamic recovery which leads to a decreasing hardening rate. Stage 4 often appears with a linear hardening rate. Stage 1 does not appear if several slip systems are already activated at the start and is not considered in Figure 15, which shows schematic flow curves for stages 2 to 4. The different stages most easily distinguished in Figure 15(b). The relevant stage for simulations in the present thesis is stage 3, and the applied models are designed to describe this stage [19].

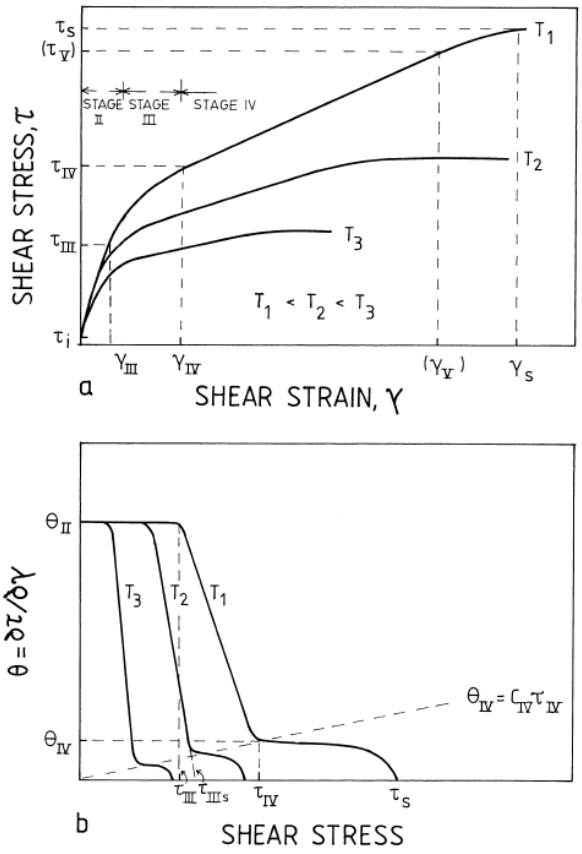

Figure 15: Deformation stages in polycrystalline fcc metals: (a) schematic stress-strain curves, and (b) strain hardening (Θ) vs shear tress (τ) curves. [19]

3.1.1. Dislocation density evolution (ABC-model)

The evolution of the dislocation density ρ over strain (i.e. over time for constant strain rate) can be described by the following evolution equation:

$$\frac{d\rho}{d\varepsilon} = \frac{d\rho^{+}}{d\varepsilon} - \frac{d\rho^{-}}{d\varepsilon} \tag{21}$$

with $\left(\frac{\rho^{+}}{d\varepsilon}\right)$ being the dislocation production (hardening) term, and $\left(\frac{\rho^{-}}{d\varepsilon}\right)$ being the dislocation annihilation (softening) term.

In MatCalc a physically-based model for the substructure evolution is implemented describing the effects of work hardening and recovery. This so called "*ABC*-model" is based on the one parameter model by Kocks [20], and is described in the work of Sherstnev et al. [21] and Buken et al. [22]. In the following sections, a short summary of the basic concept of the *ABC*-model is presented.

Hardening term

When assumed that mobile dislocations travel a mean free path, *L,* before they get immobilized or annihilated, the increase of the dislocation density ρ can be expressed as [23]:

$$\frac{d\rho}{dt} = \frac{M\dot{\varphi}}{b\,L} \tag{22}$$

where M is the Taylor factor (M=3.06 for fcc crystals [24]), $\dot{\varphi}$ is the plastic strain rate and b is the burgers vector. The mean free path is limited by the average distance between dislocations:

$$L = \frac{A}{\sqrt{\rho}} \tag{23}$$

with A being a material constant.

Softening term

If dislocations are annihilated, the dislocation density is reduced. Spontaneous annihilation occurs when dislocations with antiparallel Burger's vectors are getting closer to each other than a critical distance. This relation can be written as [25]:

$$\frac{dp}{dt} = -B\,2\frac{d_{\mathrm{ann}}}{b}\rho M\dot{\varphi} \tag{24}$$

In equation (24), d_{ann} is the critical distance as given by Brinckmann [26] and B is a parameter associated with the number of activated slip planes. The critical distance is given by equation (25), where G is the shear modulus of the matrix material, ν is the Poisson's ratio and $Q_{\mathrm{v}}^{\mathrm{f}}$ is the vacancy formation energy.

$$d_{\mathrm{ann}} = \frac{Gb^4}{2\pi(1-\nu)Q_{\mathrm{v}}^{\mathrm{f}}} \tag{25}$$

A model suggested by Lindgren et al. [23] describes recovery by dislocation climb. With the assumption that the self-diffusion coefficient along dislocations D_{d} (pipe-diffusion) controls the thermally activated climb, dislocation density evolution due to this effect is given by equation (26) [27].

$$\frac{d\rho}{dt} = -C2D_{\mathrm{d}}\frac{Gb^3}{k_{\mathrm{B}}T}\left(\rho^2 - \rho_{\mathrm{eq}}^2\right) \tag{26}$$

In equation (26), k_{B} is the Boltzmann constant, T the absolute temperature, ρ_{eq} the equilibrium dislocation density ($\rho_{\mathrm{eq}} = 10^{11}$) and C is a calibration parameter, which takes into account the solute trapping.

3.1.2. Work hardening

The influence of the dislocation density on the mechanical properties of the material (i.e. strength) is taken into account via equation (27) as suggested by Taylor [28]:

$$\sigma = \sigma_0 + \alpha M b G \sqrt{\rho} \tag{27}$$

where ρ is the average dislocation density, α is a constant proportionality factor ($\alpha \approx 0.5$), and σ_0 is the basic strength and other strengthening effects.

3.2. Modelling of grain-structure evolution

The grain structure is characterized by the size and shape of the individual grains in the matrix. The presented model neglects the shape of grains and assumes a mean grain size and a spherical shape of all grains. The approaches, to describe important processes for the grain structure evolution, are presented in the following.

3.2.1. Recrystallization

The process of recrystallization is expressed in terms of nucleation and growth kinetics. The models used to describe these two processes are presented in the following sections.

Nucleation

Nuclei for recrystallization generally emerge at the junctions of high-angle grain boundaries (HAGB) and low-angle grain boundaries (LAGB) as described by the Bailey-Hirsch mechanism [7]. Therefore, the nucleation rate, $\dot{N}_{\mathrm{rx}}$, is written as

$$\dot{N}_{\mathrm{rx}} = \begin{cases} C_{\mathrm{rx}} \left(\frac{\pi}{6}\delta^2 D\right)^{-1} \exp\left(\frac{Q_{\mathrm{rx}}}{RT}\right)(1 - X_{\mathrm{rx}}) \ , & \delta \geq \delta_{\mathrm{crit}} \\ 0 \ , & \delta < \delta_{\mathrm{crit}} \end{cases} \tag{28}$$

where δ is the subgrain diameter, D is the mean unrecrystallized grain diameter, C_{rx} is a calibration coefficient, Q_{rx} is an activation energy (which is similar to the activation energy of substitutional self-diffusion along grain boundaries), X_{rx} is the recrystallized fraction, and R is the universal gas constant. The occurrence of nucleation is determined by the ratio between surface energy of a subgrain, γ_{LB}, and the driving force for recrystallization, P_{D}, which is provided by the excess of deformation-induced dislocations. This correlation is described by Huang and Humphreys [29]. The critical subgrain diameter δ_{crit} is given by equation (29).

$$\delta_{\mathrm{crit}} = \frac{3\gamma_{\mathrm{LB}}}{P_{\mathrm{D}}} = \frac{3\gamma_{\mathrm{LB}}}{0.5 G b^2 \rho} \tag{29}$$

Although the subgrain diameter and its evolution is described by a mean value (within the framework of a single class model), a Rayleigh size distribution for the subgrain diameter is

assumed. [30] Thus, even if the average subgrain size is below the critical diameter for nucleation of new grains, some subgrains in the size distribution may be large enough to cause nucleation, which is illustrated in Figure 16.

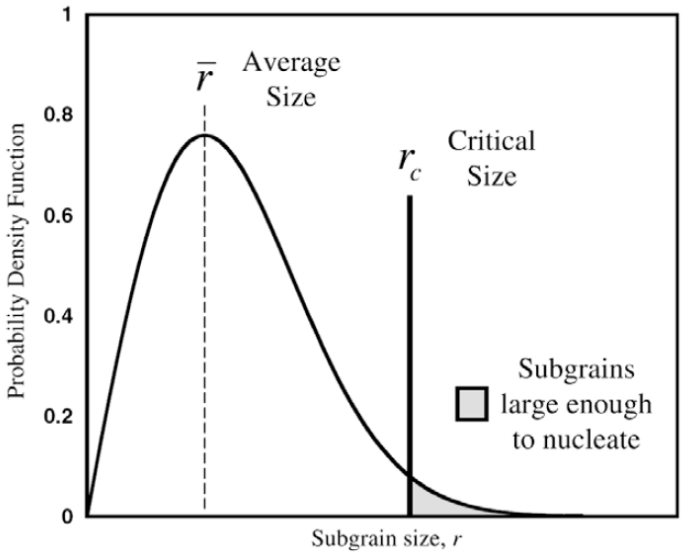

Figure 16: The subgrain size distribution within each grain of average radius $\bar{r}$. The shaded area represents the fraction of subgrains larger than the critical size r_c. [30]

Grain size evolution of recrystallized grains

When a nucleus exceeds the given critical size, its further growth rate, $\dot{D}_{\mathrm{rx}}$, is described by an effective HAGB-mobility, $M_{\mathrm{eff,HB}}$, and the driving force P_{D} as

$$\dot{D}_{\mathrm{rx}} = M_{\mathrm{eff,HB}} P_{\mathrm{D}} (1 - X_{\mathrm{rx}}) \tag{30}$$

The growth velocity of recrystallizing grains is assumed to decrease with decreasing unrecrystallized volume available.

Recrystallized volume fraction

The evolution of the recrystallized volume fraction is described as superposition of nucleation of newly recrystallized grains and the growth of existing ones with the following equation:

$$\dot{X}_{\mathrm{rx}} = \frac{\pi}{6}\left(\dot{N}_{\mathrm{rx}} D_{\mathrm{rx}}^3 + 3 N_{\mathrm{rx}} \dot{D}_{\mathrm{rx}} D_{\mathrm{rx}}^2\right) = \frac{\dot{V}_{\mathrm{rx}}}{V_{\mathrm{tot}}} \tag{31}$$

where $\dot{V}_{\mathrm{rx}}$ is the velocity of recrystallized volume gain and V_{tot} is the total volume.

The dislocation density evolution is described by an extended Kocks-Mecking model as described in section 3.1., except for a change in the last term of the equation which describes

the static recovery. In the original model of Sherstnev et al. [20] it is assumed that the driving force for static recovery is given by the difference of actual and equilibrium dislocation density. Here a limiting degree of static recovery is given by the amount of geometrically necessary dislocations, ρ_{RS}, needed for maintaining the subgrain microstructure. According to the model of Read-Shockley [31], which is used here, the mean subgrain misorientation angle, θ_{mean},and the mean subgrain size, δ, in a periodic network in the grain boundary plane, define the required dislocation density, ρ_{RS}, as

$$\rho_{RS} = \frac{\tan(\theta_{\mathrm{mean}})}{b\delta} \tag{32}$$

The deformation-induced subgrain size is connected with the dislocation density via the principle of similitude.[32][33] This mainly empirical principle delivers a cell/subgrain size, which is linked to the dislocation density evolution during deformation with

$$\delta = \frac{K}{\sqrt{\rho}} \tag{33}$$

where K is a material parameter. To describe the coarsening of subgrains that takes place after deformation but before the staring of recrystallization the following expression is used:

$$\dot{\delta} = M_{\mathrm{eff,LB}} \frac{3\gamma_{\mathrm{LB}}}{\delta} \tag{34}$$

where $M_{\mathrm{eff,LB}}$ is the effective LAGB mobility.

3.2.2. Growth

The model for grain growth is very similar to the one used for the growth of recrystallized grains, mentioned above. It also operates with a Mobility and a Driving force/pressure term. The general equation that describes the evolution of grain size is

$$\dot{D} = \frac{dD}{dt} = MP_{\mathrm{D}} \tag{35}$$

where $\dot{D}$ is the grain size growth rate, M the grain boundary mobility, and P_{D} is the driving force.

Driving force

The driving force for grain growth is dependent on the Grain interface energy and the grain size. This correlation is described by the following equation:

$$P_D = 2k_{\mathrm{d}}\frac{\gamma_{\mathrm{HA}}}{D} \tag{36}$$

with γ_{HA} being the grain interface energy, *D* the mean grain size (diameter) and k_{d} is a scaling factor.

Boundary mobility

The grain boundary mobility is described by

$$M = M_0 \exp\left(-\frac{Q}{RT}\right) \tag{37}$$

where M_0 is a pre-factor, and *Q* is the activation energy for grain boundary movement. If there are no obstacles for the growing grains in the material, the mobility term, in this case called M_f, is described by the Turnbull Mobility [34] and a scaling factor η_f.

$$M_{\mathrm{f}} = \eta_{\mathrm{f}} M_{\mathrm{TB}} \tag{38}$$

here, M_{TB} is the Turnbull-Mobility given by

$$M_{\mathrm{TB}} = \frac{\omega D_{\mathrm{GB}} V_{\mathrm{m}}}{b^2 RT} \tag{39}$$

where ω is the grain boundary width (normally a value of 1nm is assumed), D_{GB} is the diffusion coefficient for grain boundaries and V_{m} the molar volume [35]. If precipitates are present in the system or solute drag occurs additional forces and mobilities are introduced. Namely the pinning force, P_{Z}, the grain boundary mobility with solute drag M_{sd}, the grain boundary mobility for a matrix with precipitates, M_{prec}, and the effective grain boundary mobility M_{eff}. M_{eff} is assumed to be mainly determined by three partial mobilities, M_{free}, M_{pinned} and M_{SD}:

$$M_{\mathrm{free}} = \eta_{\mathrm{free}} M_{\mathrm{TB}} = \eta_{\mathrm{free}} \frac{\omega D_{\mathrm{GB}} V_{\mathrm{m}}}{b^2 RT} \tag{40}$$

with η_{free} beeing a linear pre-factor, ω is the grain boundary width and is M_{TB} is the Turnbull mobility [34]. The pinned mobility is expressed as:

$$M_{\mathrm{pinned}} = \eta_{\mathrm{pinned}} M_{\mathrm{free}} = \eta_{\mathrm{pinned}} \eta_{\mathrm{free}} M_{\mathrm{TB}} \tag{41}$$

with a dimensionless pre-factor, η_{pinned}. Alloying elements in metals can have two effects on recrystallization kinetics: Zener pinning by particles and solute drag by solid solution atoms. [36] To describe the effect of precipitates, the Zener pressure, P_{Z}, can be written [37] as

$$P_{\mathrm{Z}} = \frac{3f\gamma_{\mathrm{HB}}}{2r} \tag{42}$$

where f is the precipitated phase fraction and r is the mean precipitate radius. Since MatCalc can calculate size distribution of precipitates, a precipitate size distribution dependent model for the Zener pressure can be used. This size class-based model as introduced by Rath and Kozeschnik [38], and takes different precipitate types, *i*, and size classes, *k* , into account. To describe the influence of these precipitates equation (43) is used:

$$P_{\mathrm{Z}}(k,i) = \frac{3}{2}\gamma_{\mathrm{HB}} \sum_{i} \sum_{k} \frac{f_{k,i}}{r_{k,i}} \tag{43}$$

It is assumed that the precipitates, which potentially pin the boundaries of recrystallizing grains, are interconnected along high-velocity diffusion paths, i.e., the grain boundaries. The coarsening of these precipitates is accelerated due to the fast diffusion along these boundaries. Coarsening leads to a decrease in number density of precipitates which pin the grain boundaries. Therefore, the Zener pressure is reduced, which means that the grain boundary becomes locally released. This free boundary then moves further into the deformed microstructure until it is again pinned by a new front of precipitates. Then the local coarsening starts again, and this cycle repeats itself. On average, the grain boundary can therefore continuously move through the material although the Zener pressure determined by the initial precipitate distribution exceeds the driving pressure for recrystallization [22]. This special case of precipitate coarsening behaviour was experimentally observed by Yazawa et al. [39] and Jones and Ralph [40]. To describe this mechanism in a model, the Zener pressure is included into the mobility term instead of reducing the driving force by the Zener pressure to obtain an effective driving force. The mobility resulting out of this assumption, which takes the particle pinning effect into account is described with equation (44).

$$M_{\mathrm{prec}} = \begin{cases} \left(\frac{P_{\mathrm{D}} - P_{\mathrm{Z}}}{P_{\mathrm{D}}}\right) M_{\mathrm{free}} + \left(1 - \frac{P_{\mathrm{D}} - P_{\mathrm{Z}}}{P_{\mathrm{D}}}\right) M_{\mathrm{pinned}} & , P_{\mathrm{D}} > P_{\mathrm{Z}} \\ M_{\mathrm{pinned}} & , P_{\mathrm{D}} \leq P_{\mathrm{Z}} \end{cases} \tag{44}$$

where M_{prec} is the effective mobility of the grain boundaries in the presence of precipitates, M_{free} ist he free mobility without any dragging and retarding influences of particles and/or solute atoms and M_{pinned} is the limiting (non-zero) mobility, which is adopted by the grain boundary when the Zener pressure exceeds the driving pressure for recrystallization. The effect of solute drag is included into the model on the basis of the work of Cahn. [41] The dragging effect of solute atoms, which are segregated into the grain boundary, is put into the mobility term:

$$M_{\mathrm{SD}} = \frac{1}{\alpha C_{\mathrm{GB}}} \tag{45}$$

with M_{SD} being the mobility of the grain boundary in the presence of solute drag. C_{GB} is the grain boundary concentration of the solute drag element, and α is an inverse mobility which gives the temperature dependency of the solute drag effect via the grain boundary/atom interaction energy, E_{B}, given by:

$$\alpha = \frac{\omega (RT)^2}{E_{\mathrm{B}} D_{\mathrm{CB}} V_{\mathrm{M}}} \left(\sinh\left(\frac{E_{\mathrm{B}}}{RT}\right) - \left(\frac{E_{\mathrm{B}}}{RT}\right) \right) \tag{46}$$

where V_{M} is the molar volume of the matrix phase, ω is the grain boundary width and D_{CB} is the cross-boundary diffusion coefficient of the solute drag element. Finally, the integral effective mobility is given by equation (47).

$$M_{\mathrm{eff,HB}} = \left(\frac{1}{M_{\mathrm{prec}}} + \frac{1}{M_{\mathrm{SD}}} \right)^{-1} \tag{47}$$

4. Simulation and Results

4.1. Simulation setup

To practically set up a simulation, one has to carry out a series of different tasks, which are shortly described in the following sections, and detailed information on the specific setup applied for the different simulations is given.

4.1.1. Thermo-kinetic system definition: Composition, phases and databases

In a first step the necessary thermodynamic and diffusion (mobility) databases have to be loaded into the system, and the chemical composition for the investigated alloy has to be defined. Table 5 shows the chemical composition for the investigated alloys.

Table 5: Chemical composition of the investigated alloys

Element (wt.-%)	Ni	Al	Co	Cr	Fe	Mo	Nb	Ti	W
Inconel 625	balanced	0.4	1.0	22.0	5.0	9.0	4.0	0.4	---
Inconel 718	balanced	0.55	0.3	17.6	20.7	2.9	5.2	1.1	---
Rene 65	balanced	2.13	13.0	16.0	1.0	4.0	0.7	3.7	4.0
Rene 88DT	balanced	1.77	13.0	16.0	---	4.0	0.7	4.0	4.1

The next step is to choose the phases that should occur in the simulation. At this point matrix and possible thermodynamic phases should be defined. For the R-65 and R-88DT alloy two phases were defined, namely the nickel-matrix and the precipitation phase y'. For the IN-718 alloy, in addition to the two already mentioned phases, the y'' and the delta phase were defined. Table 6 gives an overview over the active phases during simulation for the different alloys.

Table 6: Selection of the thermodynamic equilibrium phases

Alloy	Active phases during simulation			
Inconel 625	FCC_A1	---	---	---
Inconel 718	FCC_A1	GAMMA_PRIME	GAMMA_DP	DELTA
Rene 65	FCC_A1	GAMMA_PRIME	---	---
Rene 88DT	FCC_A1	GAMMA_PRIME	---	---

For the simulation studies in the present thesis the latest MatCalc databases available were used.

4.1.2. Precipitation domain

Parameters which are specific for the investigated material have to be entered into the calculation software. These are physical and mechanical parameters like the Young's modulus, quantities that characterize the microstructure like grain size, and simulation parameters that are needed to calibrate models like the ABC-model.

The microstructural parameter used as input for the simulation are given in Table 7. The initial grain size has been determined experimentally for IN-718 and Rene 65 alloy, and taken from literature for Rene 88DT alloy. The other parameters have been assumed reasonable, for example the subgrain diameter was chosen as an eight of the grain diameter for all alloys.

Table 7: Microstructural parameter

Parameter	IN-718	IN-625	Rene 65	Rene 88DT
Grain diameter [µm]	55	---	10	10
Subgrain diameter [µm]	6.875	---	1.25	1.25
Equilibrium dislocation density [m^{-2}]	1e11	1e11	1e11	1e11
Cell wall width [m]	1e-10	---	---	---

To find appropriate simulation parameters for the substructure evolution model, literature which contains experimental results concerning stress-strain curves, has been investigated. Some Papers, which met the necessary requirements, like adequate description of investigated material concerning the microstructure, and the applied mechanical treatment, were taken as basis for the adjustment of the parameter for the *ABC*-model, which describes the evolution of the dislocation density (section 3.1.1). For the determination of *A* and *B* parameter, deformation experiments at room temperature were taken as source for the parameter adjustment. The *C* parameter cannot be obtained from experimental data valid at room temperature, because it becomes only relevant at elevated temperatures. The experimental data, for stress-strain curves at higher temperatures found in literature are often far apart from each other, which can be explained due to the differences in the processing history of the samples. Therefore, the *C* parameter for the room temperature simulation, was estimated based on existing values for microalloyed steel from Buken and Kozeschnik [22]. The recovery described by the *C*-term should be far lower in Ni-based superalloys and was therefore assumed to be approx. 1e-7. The *ABC* parameter for the other alloys, namely IN-600 and IN-625, were determined in the same manner, and compared to each other to investigate the effect of the chemical composition and heat treatment condition on the choice of the *A* and *B* parameter. The parameters that were found to be suitable for substructure simulation are shown in Table 8.

Table 8: Parameters for the substructure evolution model

Parameter	IN-718	IN-625
A	30 - 40	55 - 65
B	3.3	1.0
C	0.5e-7	1e-7
A' (similitude Parameter)	60	60

The parameter *A* depends on temperature, strain rate and the initial microstructure of the sample and therefore is not a rigid value, but has to be adjusted if one of these parameters changes. The same applies to *B* but in the framework of this thesis a fixed value for every alloy was sufficient.

For the simulation of the grain-structure evolution, additional parameters have to be defined. The parameters for the grain boundary mobility model used for the simulation of IN-718 alloy are shown in Table 9, and the grain boundary energy is assumed to be 0.7 J/m².

Table 9: Parameters for the grain boundary mobility model used for IN-718 alloy

Parameter	IN-718
Mobility correction factor HAGB	0.001
Solute drag mobility corr. factor HAGB	100
Pinned mobility corr. factor HAGB	0.001
Mobility correction factor LAGB	1
Pinned mobility corr. Factor for LAGB	0.01

The matrix diffusion enhancement factor, is a variable in the thermokinetic software package MatCalc, which influences the values of diffusion coefficients in a linear way. It is therefore utilized, to compensate simplified assumptions, concerning simulation models, where the diffusion plays an important role. For example, the growth rate of precipitates. To further adjust the precipitation growth rate the matrix diffusion enhancement factor, was set to 0.2.

4.1.3. Precipitate phases

For an efficient and accurate precipitation kinetics simulation, the number of size classes has to be adjusted for each precipitate phase. After some tests this value was set to 100, because a larger number of size classes didn't increase the prediction quality of the simulation and therefore would only increase calculation time. To simulate the precipitation kinetics in alloy R-65, a preliminary study for parameter identification was done. As experimental basis for this

study, R-88DT alloy was chosen because firstly, it has a similar chemical composition compared to R-65 alloy and secondly, more experimental data in literature are available for R-88DT. Experimental data from Cahn [42] and Singh et al. [43] were used to compare the simulation results. The first simulation tests showed that the calculated precipitation sizes were above the experimentally observed values. To improve the simulation, parameter studies for the regular solution critical temperature, T_C , were performed. In addition, the different models for the calculation of the chemical nucleation composition were investigated. These are "ortho equilibrium", "min G*" and "maximum nucleation rate". The simulation settings for the different phases have been defined under the aspect to maximize the stability and accuracy of the simulation. Table 10 summarize these parameters which have been chosen differently than the MatCalc default values.

Table 10: Simulation Parameters for precipitation phases

Phase	Gamma-Prime	Gamma-DP	Delta
Number of size classes	100	100	100
Nucleation model	Maximum nucleation rate	Maximum nucleation rate	Orthoequilibrium
Tcrit [K]	2200	2200	2500
Shape factor	---	---	0.1

4.1.4. Thermo-mechanical treatment

Finally, in the simulation settings, the thermal or thermo-mechanical treatment has to be defined for each simulation run. In MatCalc this data can be entered using the graphical user interface (GUI) or via console commands. For example, heat/cooling rates, isothermal holding stages and deformation rates can be adjusted. Figure 17 shows a screenshot of the thermo-mechanical treatment menu in MatCalc. The "available treatment" window shows all treatments that are already defined by the user, and the "data" window shows information like start temperature, end temperature, or strain that will be accumulated during a certain segment of a treatment.

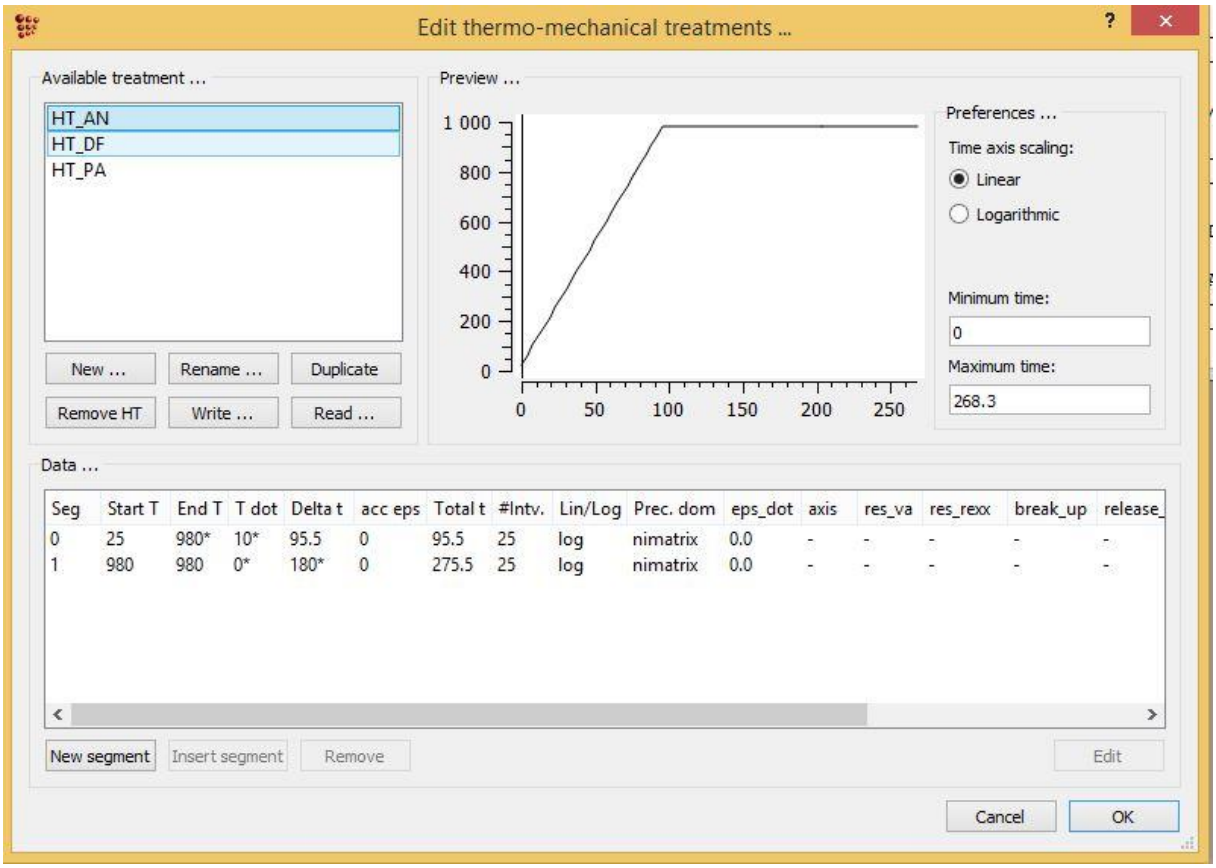

Figure 17: Screenshot from MatCalc; thermo-mechanical treatments window.

4.2. Part I: Precipitation kinetics simulation

In this chapter the relevant results from precipitation kinetic simulations, for the alloys Rene 65 and Inconel 718 are presented.

4.2.1. Case study: Rene 65

In this section, precipitation kinetic simulation results of alloy Rene 65 are presented, which includes the calculated equilibrium phase diagram and the results for evolution of the precipitation size of y' for different cooling rates.

Equilibrium phase diagram

MatCalc calculates the equilibrium phase fractions for all phases that are existent at a given temperature. This is done for each temperature in a user-defined temperature range. Figure 18 shows the equilibrium phase diagram for alloy Rene-65 which shows the equilibrium phase fractions of y', matrix, and liquid phase. The solvus temperature of the y' phase, according to the calculated diagram, is approx. 1100 °C. Between 500 °C and 900 °C the phase fraction of the y' phase is around 40%. At higher temperatures this value decreases, until the phase

completely dissolves. The solidus and liquidus temperature of this alloy is at 1300 °C and 1370 °C, respectively.

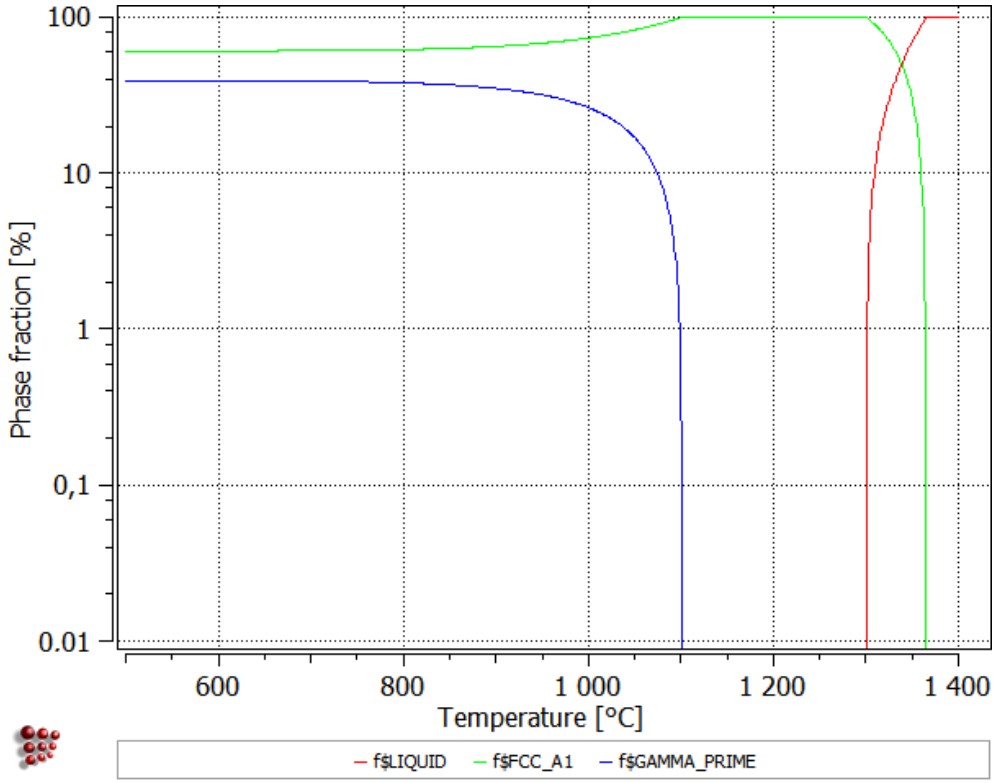

Figure 18: Calculated equilibrium phase diagram for Rene 65.

Thermo-kinetic simulation

In this simulation the cooling from solution treatment temperature with different cooling rates was investigated. The temperature of the solution treatment was set to 1150 °C. The simulation started directly with the cooling process because in the simulation the initialized state corresponds to a solution treated material. The applied cooling rates ranged from 0.1 °C/s to 50 °C/s.

The evolution of y' phase fraction, number density, and mean diameter during continuous cooling with a cooling rate of 50 °C/s, are shown in Figure 19. The phase fraction stabilizes at around 37 %. The increase of the phase fraction and number density of y' at around 8 s represents the occurrence of a secondary precipitate distribution. It is also noticed that the mean diameter (number based) rapidly decreases when the secondary precipitates form. The peak of the mean diameter at 2-3 seconds is a numerical artefact, which occurs because of assumptions which MatCalc takes concerning the starting values for precipitation size after the first nucleation.

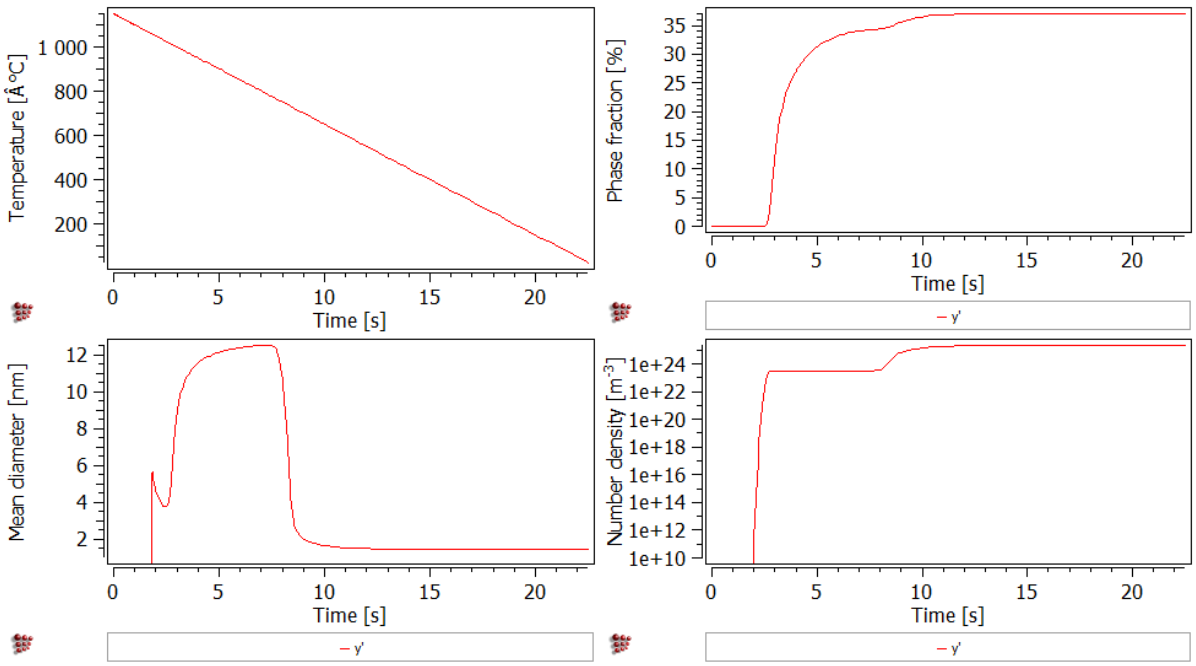

Figure 19: Temperature, phase fraction, mean diameter and number density of y' precipitates dependent on time. Cooling rate 50°C/s

Figure 20 shows the corresponding results for a cooling rate of 0.1 °C/s. In the plot for the phase fraction of y', a step at around 2800 s can be noticed in the curve of the phase fraction when the secondary precipitates form. The increase in phase fraction when the small tertiary precipitations occur is very small. The point of formation of these precipitates is best seen in a histogram (Figure 22), where all three size distributions are clearly recognizable.

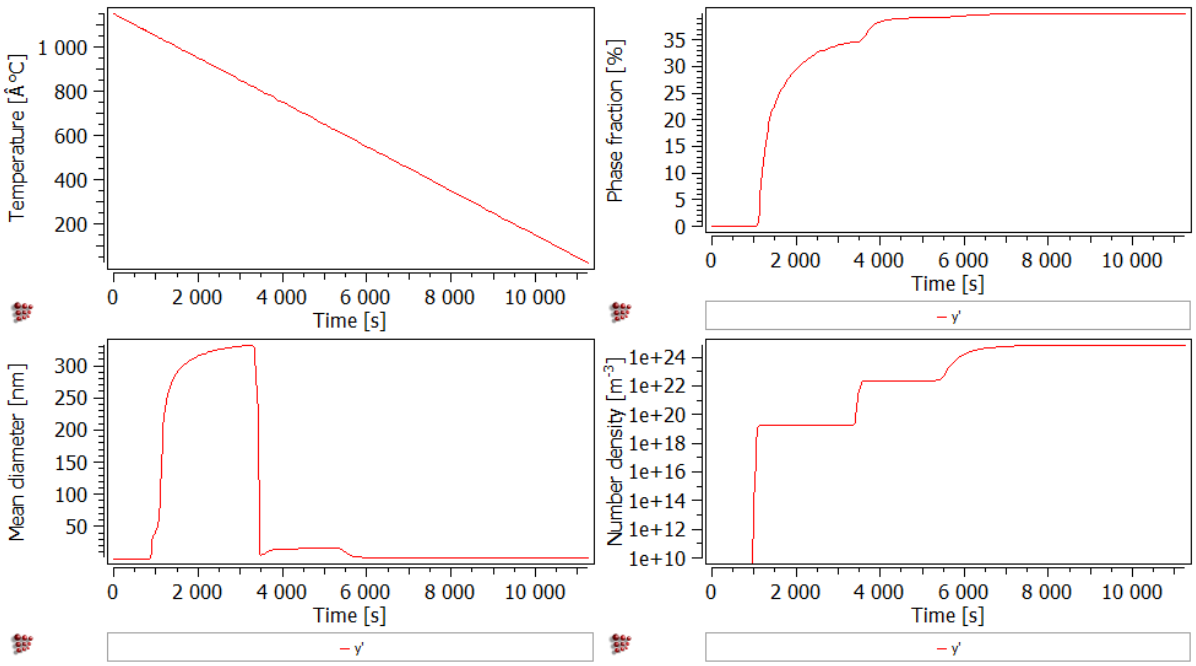

Figure 20: Temperature, phase fraction, mean diameter and number density of y' precipitates dependent on time. Cooling rate 50°C/s

The precipitate size distributions after the simulated cooling process, are exemplary shown for the highest and lowest cooling rates in Figure 21 and Figure 22. At the high cooling rate of 50 °C per second a primary size distribution at around 10 – 15 nm has formed and a second distribution where nearly all precipitates are smaller than 4 nm occurs. In contrast, for a cooling rate of 0.1 °C three distributions (primary, secondary, and tertiary) of y' are produced. The primary distribution has its mean value at around 280 nm and the secondary at around 20 nm. The precipitates of the tertiary distribution are smaller than 4 nm.

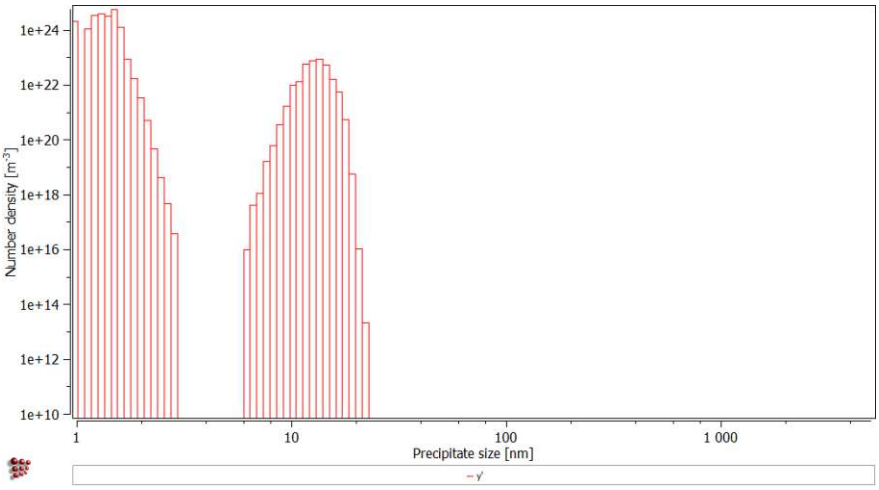

Figure 21: y' precipitate size distribution at 50°C/s cooling rate. x-axis shows diameter and y-axis number density.

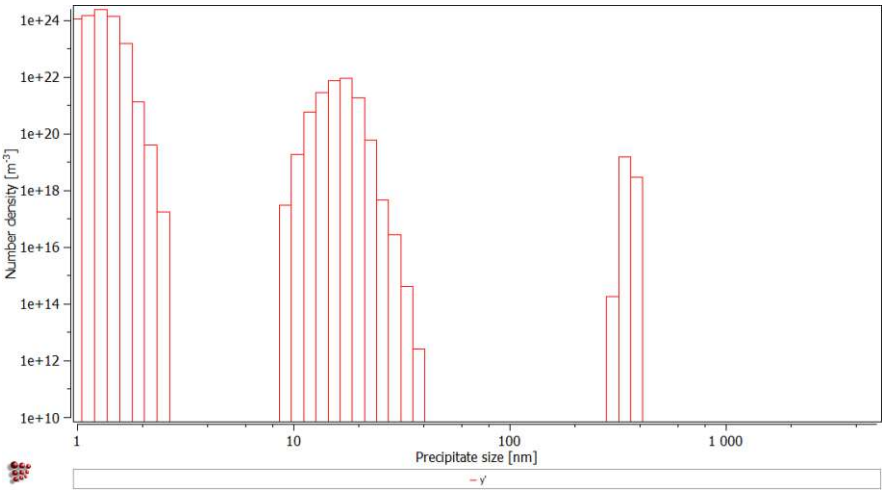

Figure 22: y' precipitate size distribution at 0,1°C/s cooling rate. x-axis shows diameter and y-axis number density.

Table 11 summarize the results of the y' precipitates for a varying of cooling rates, ranging from 0.1 °C/s to 50 °C/s. To get values for the mean diameter of primary, secondary and tertiary precipitates, the size distribution has been exported from MatCalc and evaluated with Microsoft Excel. The phase fraction of the y' phase is around 37 % for all cooling rates.

Table 11: mean diameter for primary, secondary and tertiary y' precipitates for different cooling rates.

Cooling rate [°C/s]	**Mean y' precipitate diameter [nm]**		
	primary	secondary	tertiary
0.1	290	10.0	1.5
0.3	165.0	3.0	---
1	90.0	2.0	---
5	38.0	1.0	---
10	25.0	0.3	---
50	10.0	0.1	---

4.2.2. Case study: IN-718

This chapter deals with precipitation kinetic simulations concerning the alloy IN-718 for three main precipitate phases, namely y', y'', and delta phase.

Equilibrium phase diagram

Figure 23 Figure 22shows an equilibrium sphase diagram for the alloy IN-718 which was calculated to see the equilibrium phase fractions and the solvus temperatures of the y', y'' and delta precipitates. The solvus temperature of the y' and delta phase is around 920 °C and 1050 °C, respectively. The maximum phase fraction for the y', and y'' phase is around 10 % and 12 %, respectively. The y'' phase does not occur in the stable equilibrium phase diagram, because it is a metastable phase in this. To calculate an equilibrium phase diagram which contains the y'' phase, the delta phase was suspended in MatCalc. The result is illustrated in Figure 24.

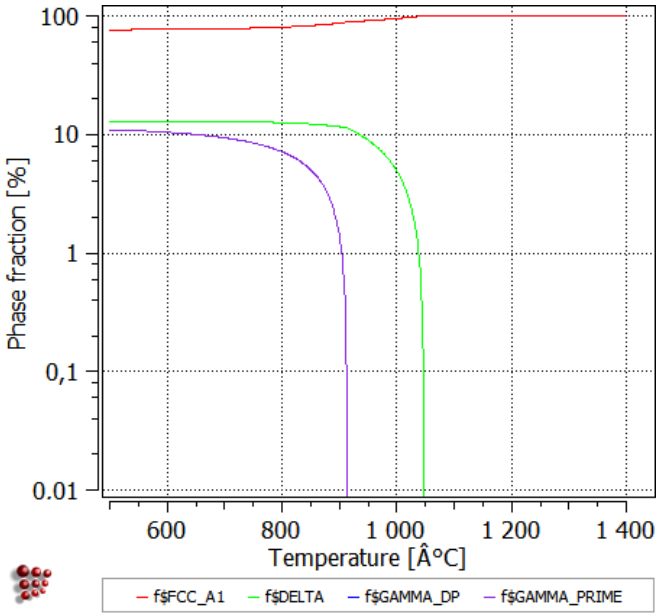

Figure 23: Calculated stable phase diagram for IN-718.

In the meta-stable phase diagram, the y' and y'' phase dissolves at around 970 °C and 940 °C, respectively. This means that the solvus of the y' is higher in the meta-stable diagram than in the stable one. The maximum phase fraction of both the y' and y'' is around 12 %, although there is slightly more y' present.

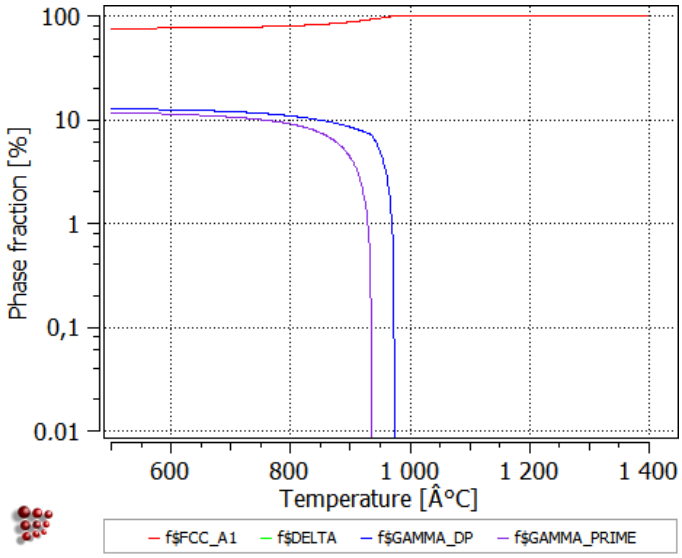

Figure 24: Calculated metastable phase diagram for IN-718.

Time-Temperature-Precipitation (TTP) diagram

The calculated TTP diagram is illustrated in Figure 25. The different curves represent the precipitation start, which is displayed for a volume fraction of 1 % for easch phase. The delta phase reaches this value at 900 °C in around 0.1 - 0.2 h. At higher or lower temperatures, it needs more time to precipitate. The temperature of fastest formation of y' and y'' is at approx. 800°C. In this simulation no y' or y'' are formed above 900 °C. The highest temperature at which the delta phase reached a volume fraction above 1 % was 980 °C.

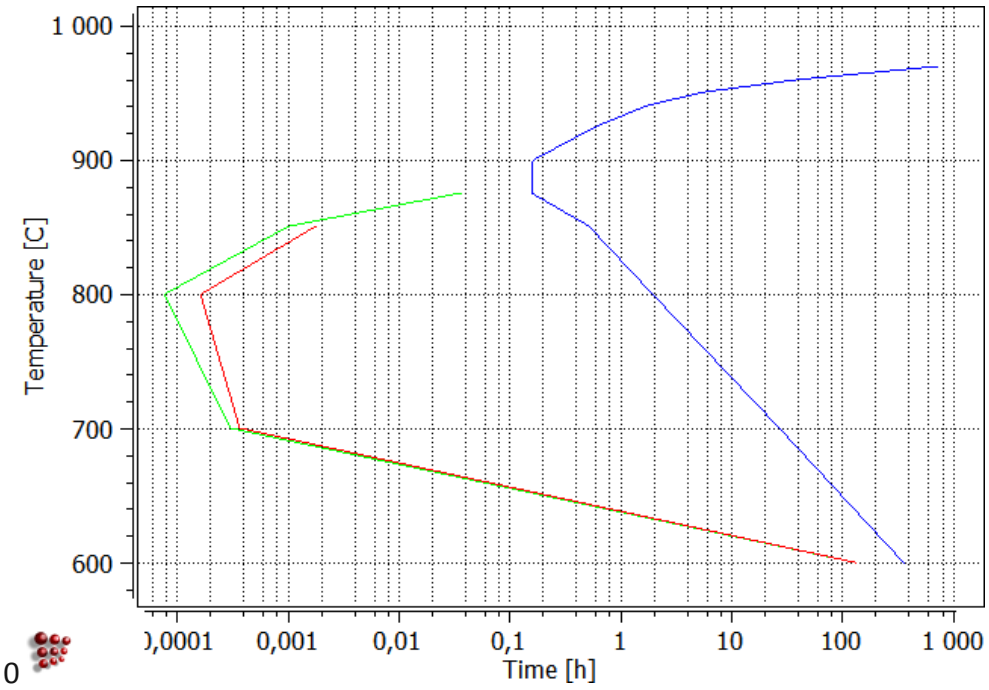

Figure 25: Calculated TTP-diagram for IN-718

4.3. Part II: Simulation of microstructure evolution

The simulation of microstructure covers the evolution of substructure and grain structure. The parameters found in preliminary studies are now applied in the simulation study on IN-718 alloy.

4.3.1. Substructure evolution

In this section the results of the preliminary study on the substructure evolution for IN-718 and for IN-625 are presented. Figure 26a shows the dislocation density at room temperature for increasing true strain up to a value of 0.6. The simulation setting for the *A* parameter of the *ABC*-model has been chosen differently to be *A* = 30 for IN-718, and to be *A* = 65 for IN-625. It can been noticed in the plot that the dislocation density for IN-718 saturates at a value of 2.3e14, whereas it is still increasing for IN-625 at maximum true strain.

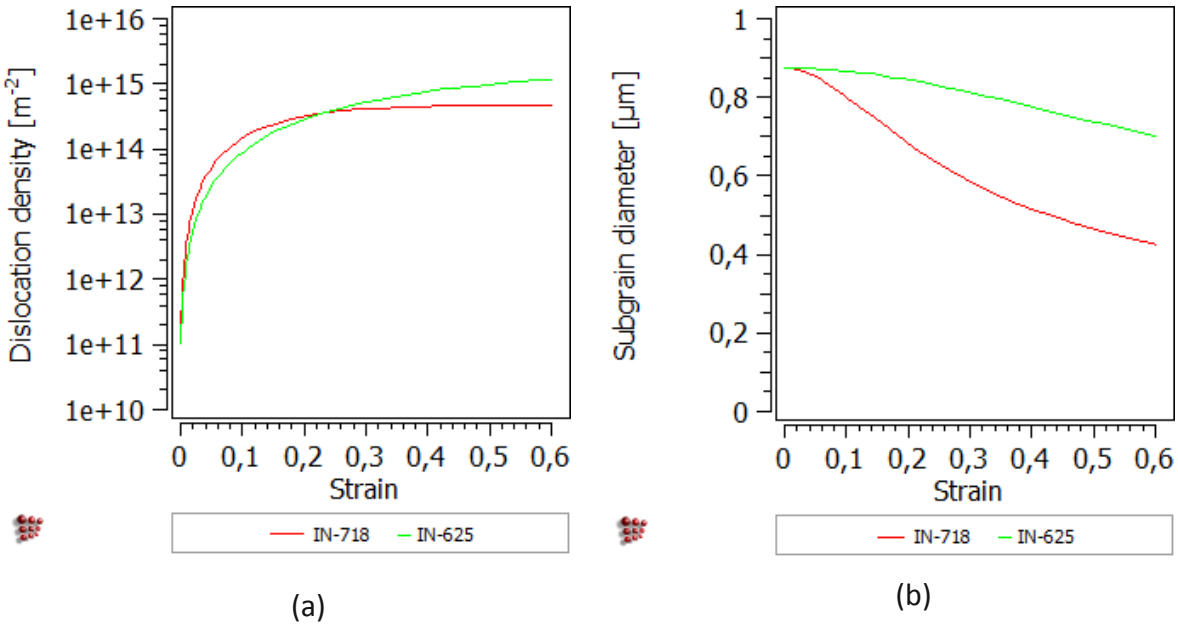

Figure 26: Evolution of (a) dislocation density and (b) subgrain diameter with true strain.

The corresponding subgrain evolution for IN-718 and IN-625 is shown in Figure 26b. While the subgrain diameter decreases only slightly in the case of IN-625, it can also be noticed that in the case of IN-718 the subgrain diameter decreases rapidly to half of the original value at maximum true strain.

4.3.2. Grain structure evolution

For the calculation of the grain structure evolution, a coupled simulation has been performed, considering the interaction of precipitates with the microstructural evolution. This case study

shows the results for the grain structure evolution for the alloy IN-718 during hot-deformation (DRX) and isothermal holding at high temperatures (MDRX). For the simulation of post-recrystallization (MDRX) after hot deformation, additional models have to be used which are described in section 3.2. The thermo-mechanical treatment for this simulation study is illustrated in Figure 27. It consist of a first segment for heating up to a certain temperature (980 °C / 1020 °C) at a rate of 10 °C/s, a segment for annealing (holding at this temperature for 180 s), a segment for deformation with a strain rate of 0.1 s^{-1} (up to a true strain level between 0.09 and 0.73), and optionally a post-heat treatment segment for isothermal holding at temperature for 15 s.

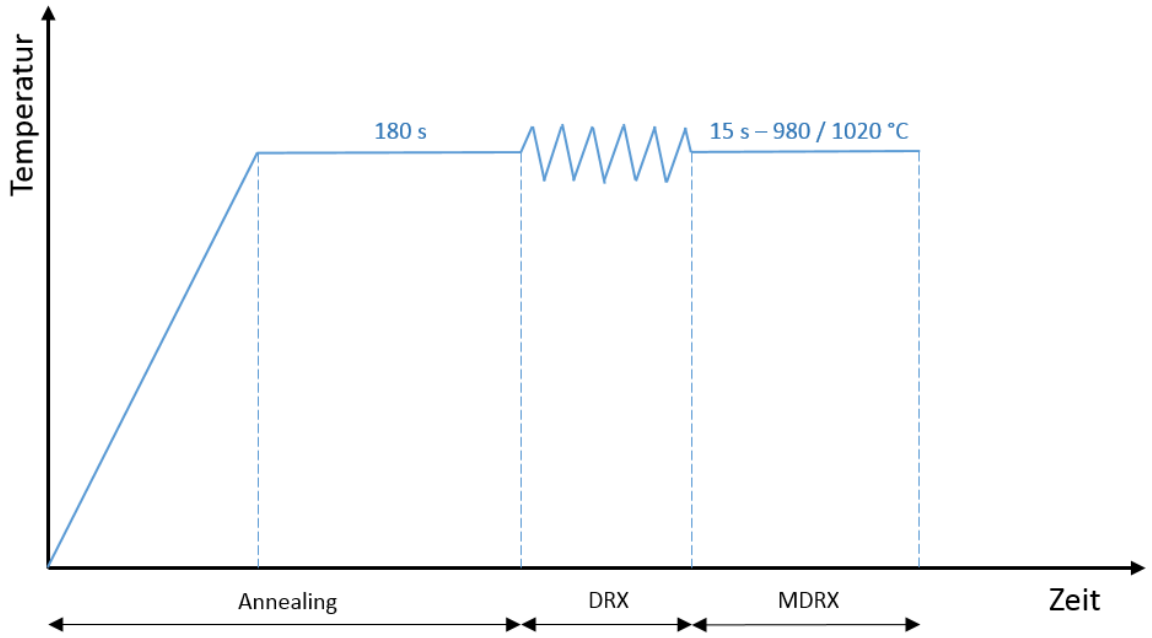

Figure 27: Heat treatment for DRX and MDRX simulation

Initial microstructure

To take the effect of precipitates in the as received material into account, precipitate size distributions for the γ', γ'' and delta phase were created within a separated MatCalc session and exported. The phase fraction for the γ'' was set to 0.13, for the δ phase to 0.02 and the γ' was assumed to have one fourth of the γ'' phase fraction. Figure 28 shows these distributions, which were imported before every recrystallization simulation. The precipitates were assumed to have a statistical normal distribution.

Table 12: Size distributions for precipitates.

Phase	Min. radius [µm]	Mean radius [µm]	Max. radius [µm]	Standard-deviation	Phase fraction
y‘	0.01	0.02	0.03	0.05	
y‘‘	0.01	0.02	0.03	0.05	
δ	1	2	3	0.05	

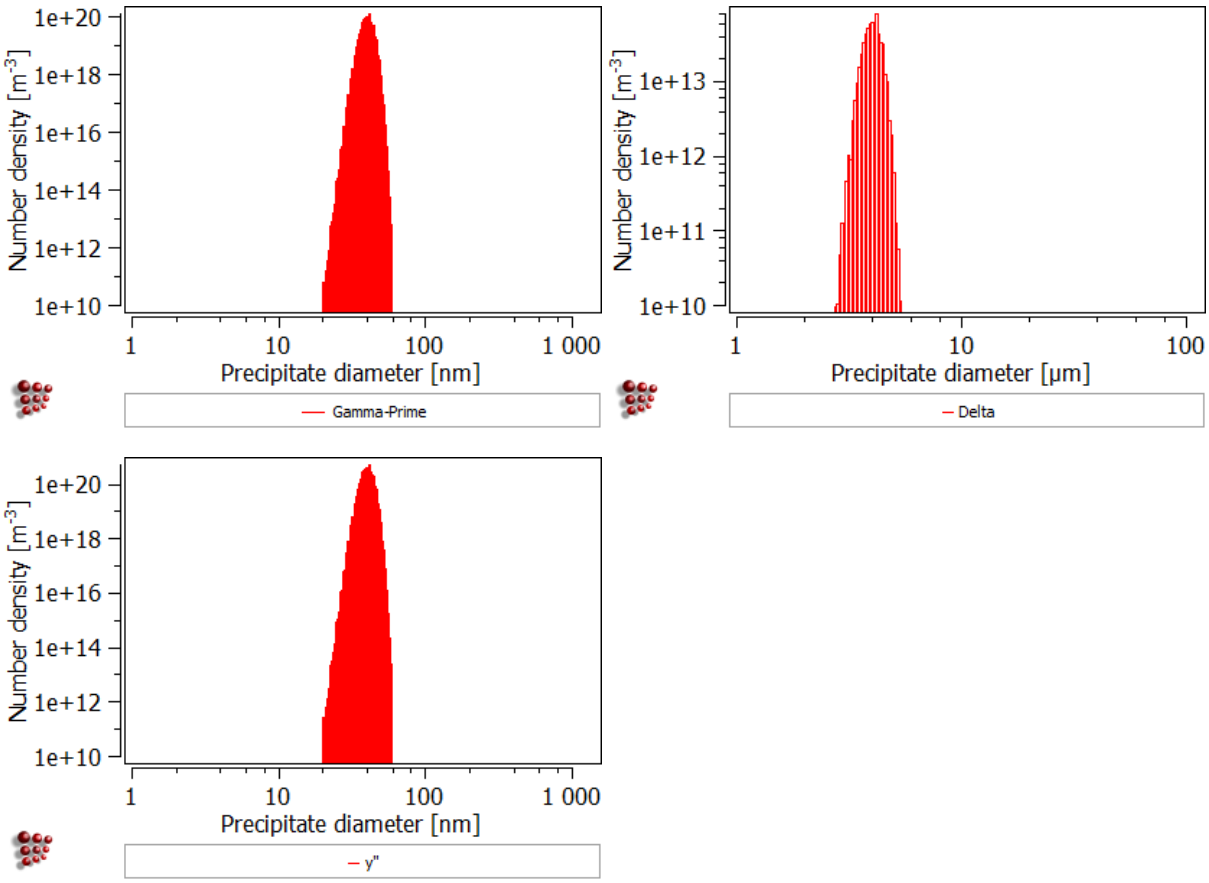

Figure 28: Precipitation distribution imported into MatCalc at the beginning of the simulation.

Stage 1: Annealing

Figure 29 exemplarily shows the evolution of the precipitates during annealing at 980 °C. While the y’, y’’ particles dissolve after 100 s, which is shortly after the heating process is finished, the delta phase stays stable. The y’ phase dissolves a little bit slower than the y’’ phase.

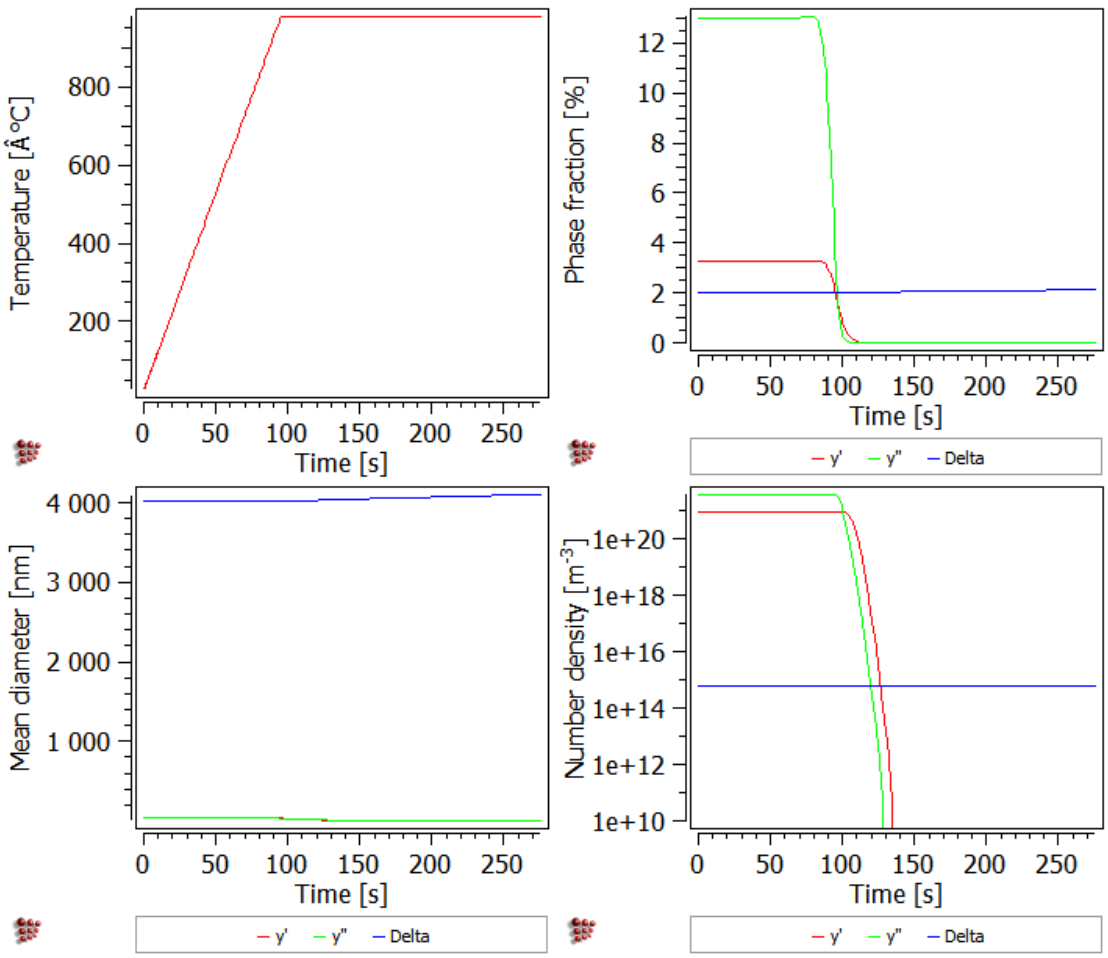

Figure 29: Evolution of precipitates during annealing.

Stage 2: Dynamic recrystallization (DRX)

In this section the evolution of the recrystallized volume fraction and grain diameter during deformation are presented. Figure 30 shows the evolution of the recrystallized volume fraction. It can be noticed that the simulated recrystallization process is slightly faster at 1020 °C than at 980 °C which agrees with theoretical expectations.

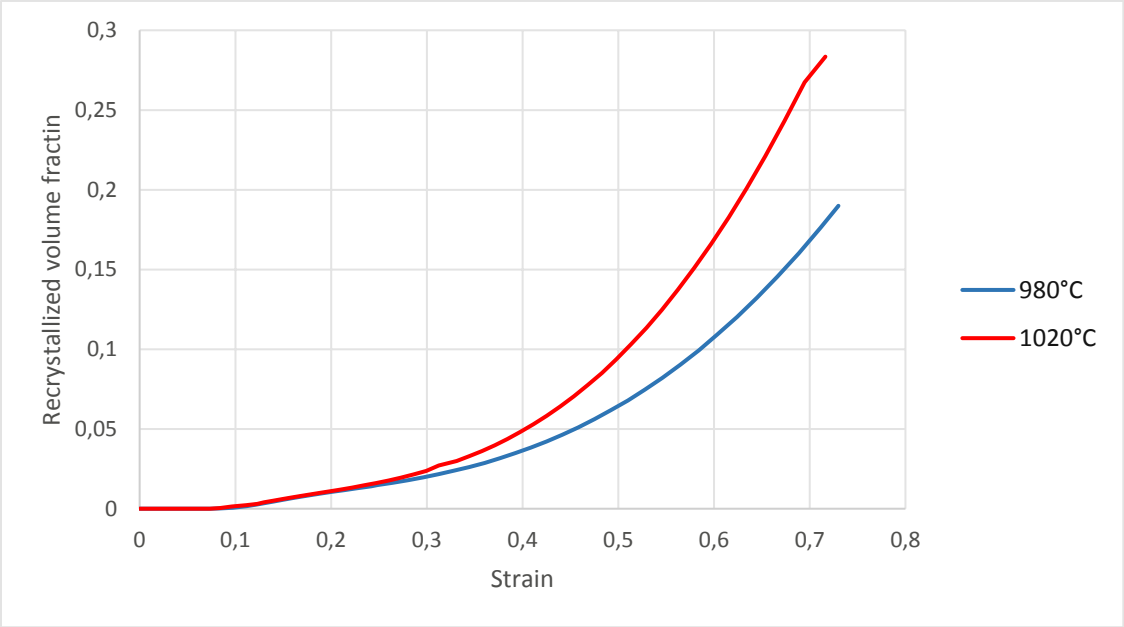

Figure 30: Evolution of recrystallized volume fraction during deformation at 980 °C and 1020 °C with a strain rate of 0.1 s^{-1} (DRX)

The grain diameter, illustrated in Figure 31 decreases with increased strain. This decrease of mean diameter is due to an increasing level of recrystallization. At a strain level of 0.73 the grain diameter at 980 °C is around 48 µm and around 44 µm for 1020 °C. The grains at the start of the curve show a little difference in size. This is due to the faster grain growth during annealing at 1020 °C when compared to 980 °C.

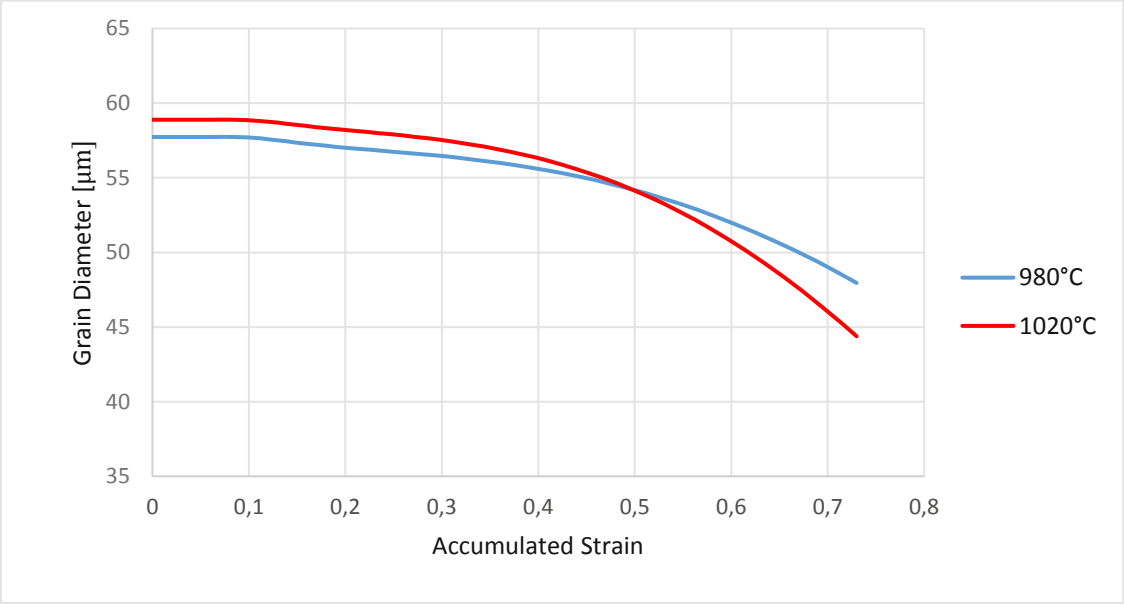

Figure 31: Evolution of mean grain diameter (area based) during deformation at 980 °C and 1020 °C with a strain rate of 0.1 s^{-1} (DRX)

Stage 3: Meta-dynamic recrystallization (MDRX)

In the case of MDRX, the recrystallization process is investigated after deformation during isothermal holding at temperature. This simulation was carried out in a separate calculation segment with input values from the DRX segment. Figure 32 and Figure 33 show the evolution of recrystallized volume fraction with time for different values of true strain. For a strain of 0.09 there is nearly no recrystallization at both temperatures. At a strain level of 0.27 recrystallization is firstly recognized to occur and reaches a value of 0.5 for 980 °C and a value of 0.65 for 1020 °C. It can be also seen that the recrystallized volume fraction after 15 s holding time approaches 1.0 for strain levels higher than 0.27 and for both temperatures.

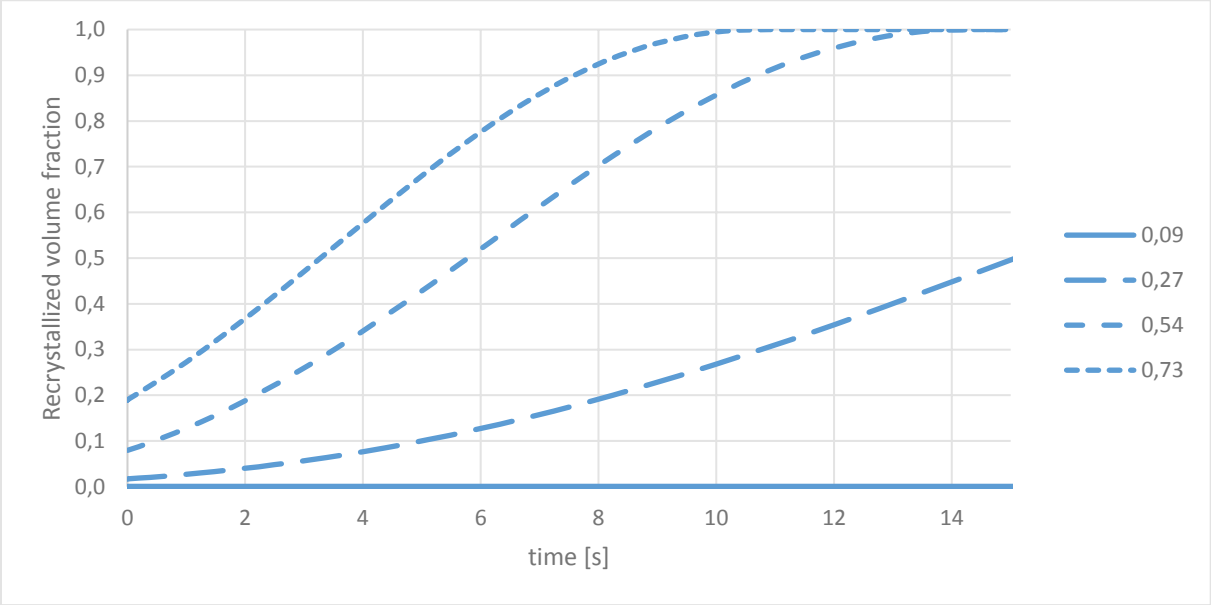

Figure 32: Evolution of recrystallized volume fraction for different true strain level for holding at 980 °C (MDRX).

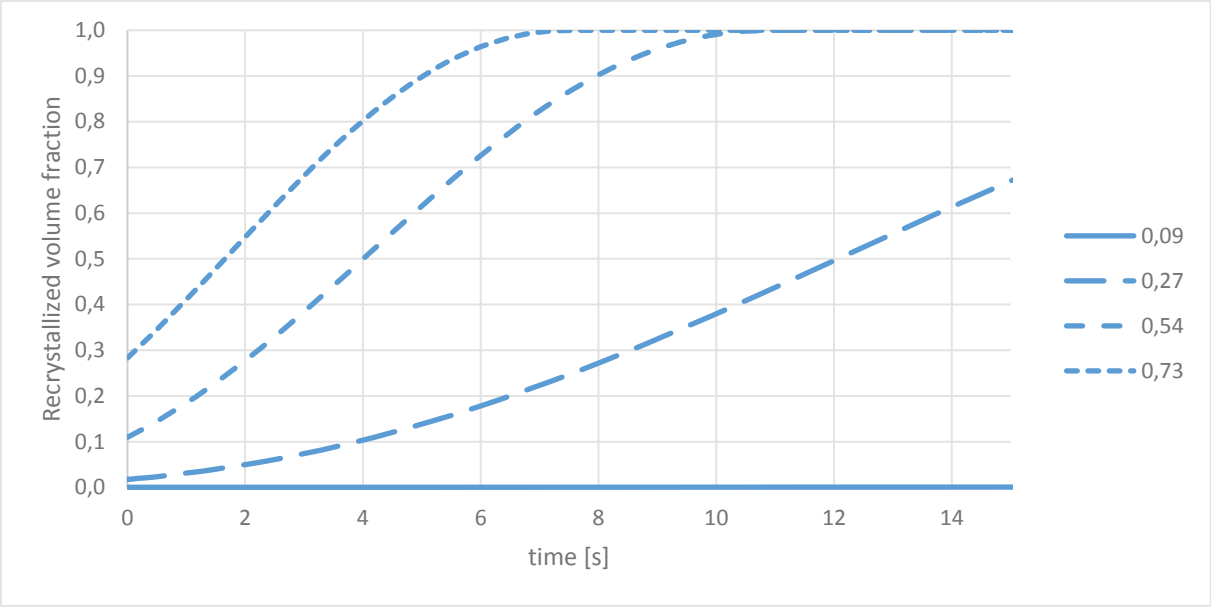

Figure 33: Evolution of recrystallized volume fraction for different true strain level for holding at 1020 °C (MDRX).

The evolution of mean grain diameters is plotted in Figure 34 and Figure 35. The grain diameters decrease faster with higher strain levels. For a true strain of 0.09 the grains keep their original size, because no recrystallization occurs. As soon as the recrystallization process starts the mean grain diameter decreases. For a strain of 0.27 a grain size of 34 µm is reached while for true strain values of 0.54 and 0.73 the mean grain size is approx. 12 µm after 15 s holding time.

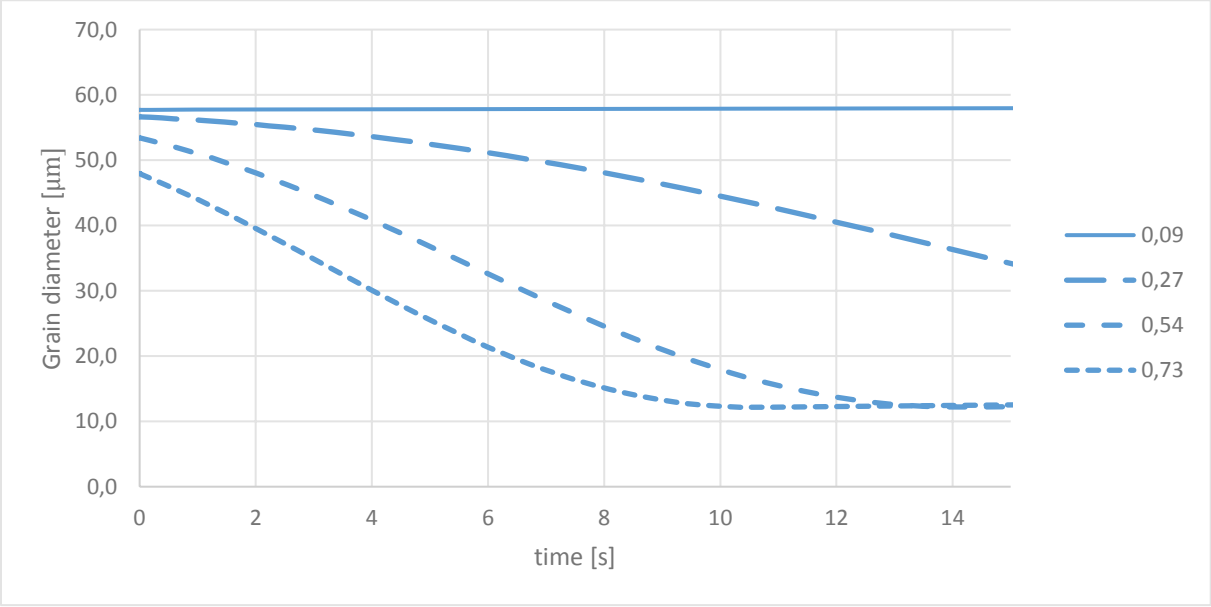

Figure 34: Evolution of the mean grain diameter (area based) for different true strain level for holding at 980 °C (MDRX)

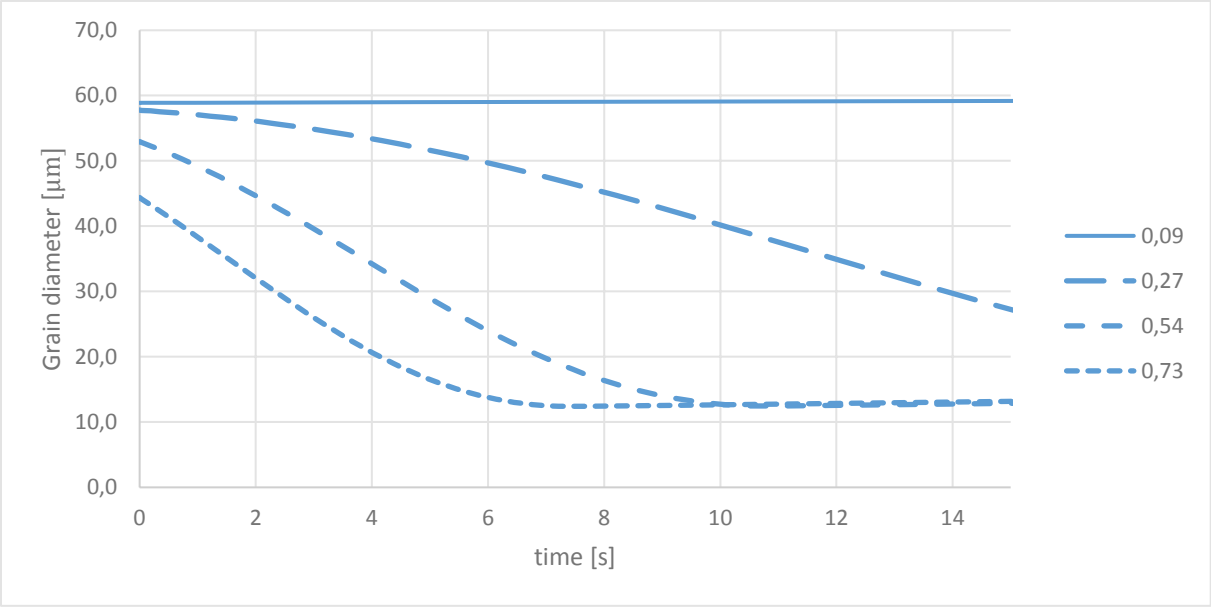

Figure 35: Evolution of the mean grain diameter (area based) for different true strain level for holding at 1020 °C (MDRX)

5. Discussion of results

In this chapter the results from chapter 4 will be discussed and some information about the preliminary studies that lead to these results will be given. Here, the precipitation kinetics and microstructure evolution simulations will be reviewed separately.

5.1. Precipitation kinetics simulation

5.1.1. Preliminary study on Rene 88DT

At the beginning of the work for this thesis a preliminary study was done to identify appropriate simulation parameters. The alloy investigated during the preliminary studies was R-88DT. Experimental results from Singh et al. [42] and Tiley et al. [43] have been used to verify the simulation results. In the work of Singh et al. [42] the precipitate evolution for different cooling rates after solution treatment has been investigated. The corresponding cooling rates water quenching (WQ), fast cooling (FC) and slow cooling (SC) has been 350 °C/s, 280 °C/s and 24 °C/s, respectively. Figure 36 shows the precipitate morphology that form at different cooling rates. At slow cooling rates the precipitates that form during the first nucleation burst are not spherical and a multi-modal size distribution finally develops. According to Figure 36 it should be assumed that the simulation delivers small monomodal precipitation distributions for very fast cooling rates and primary and secondary distribution for slower cooling rates.

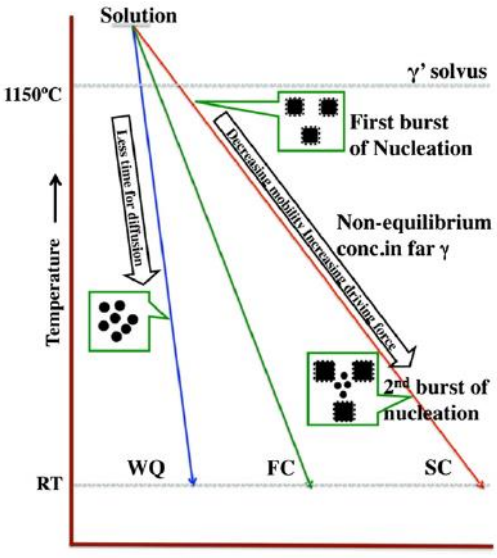

Figure 36: Schematic illustrating the effect of cooling rate on the formation of different generations of y' precipitates.[42]

Tiley et al. [43] investigated the effect of aging at 760°C after cooling with the same cooling rates as Singh et al. [42]. These works deliver information about the chemical composition of the precipitates after heat treatment. In the next section the experimental results found by Singh et al. [42] and Tiley et al. [43] are compared to the results in the preliminary simulation study.

Precipitate size distribution

Figure 37 shows the experimental TEM results from Singh et al. [42] for solution treatment at 1150 °C and slow cooling condition (350 °C/s). In this figure, the primary precipitates have a diameter of approx. 200 nm, whereas the secondary precipitates are much smaller with diameters ranging from 5 – 40 nm.

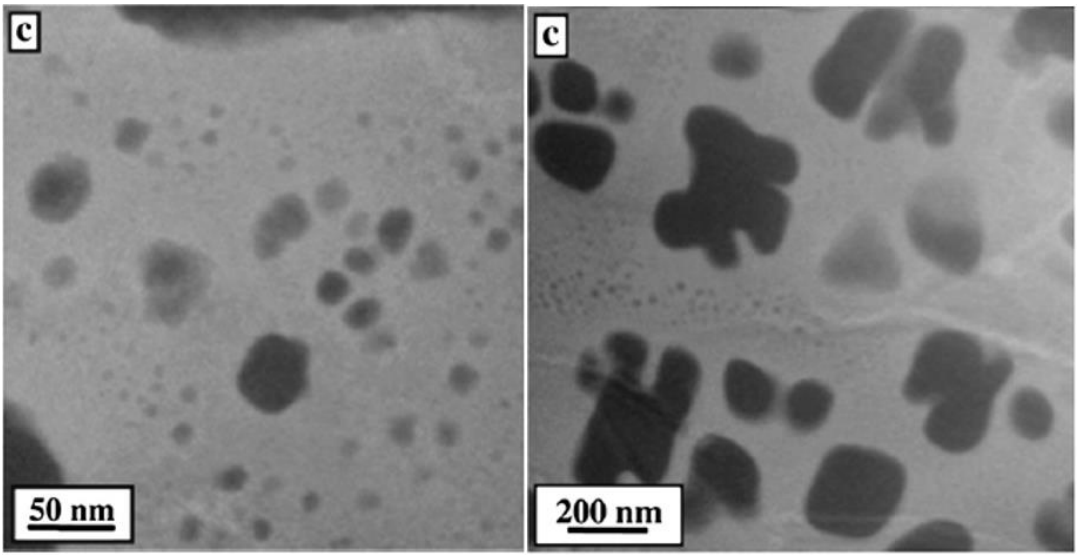

Figure 37 Energy- filtered transmission electron microscopy images obtained using Cr M-edge in the electron energy-loss spectroscopy spectrum from solutionized and slow cooled samples (SC).

For comparison with experimental results, Figure 38 shows the histogram of the y' precipitate distribution considering the same heat treatment condition (solution treatment at 1150°C / continuous cooling with rate of 350 °C/s) calculated with MatCalc employing the previous thermodynamic database (ME-NI1.1c.tdb).

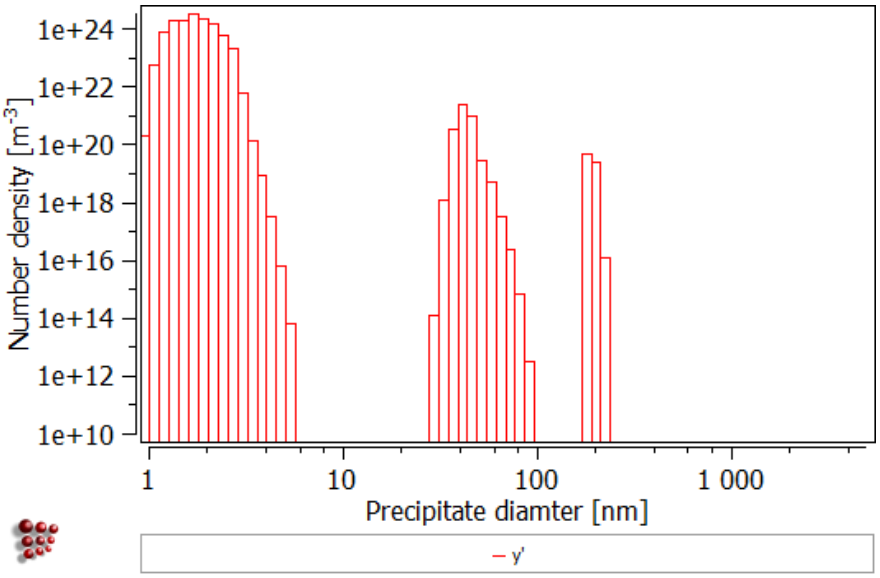

Figure 38: Size distribution of y' after SC calculated by MatCalc "old" database, x-axis: precipitate diameter

The predicted mean diameter of the primary y' is approx. 200 nm which well agrees with the experimental result from Singh et al. [42]. However, a significant deviation from the experimental results can be qualitatively noticed for the secondary y', where MatCalc predicts a precipitate diameter in the range of approx. 40 – 80 nm. Thus, to identify possible reasons for the difference between simulation and experimental results, the chemical composition of the precipitates hast been investigated more closely.

Precipitate composition

In Figure 39, the precipitate and matrix composition calculated from MatCalc is compared to experimental results from Singh et al. [42] and J. Tiley et al. [43] for quenching from solution temperature and aging at 760 °C for 50 h.

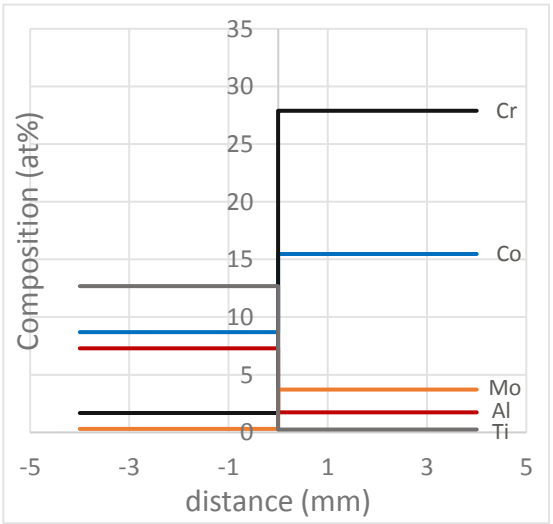

(a)

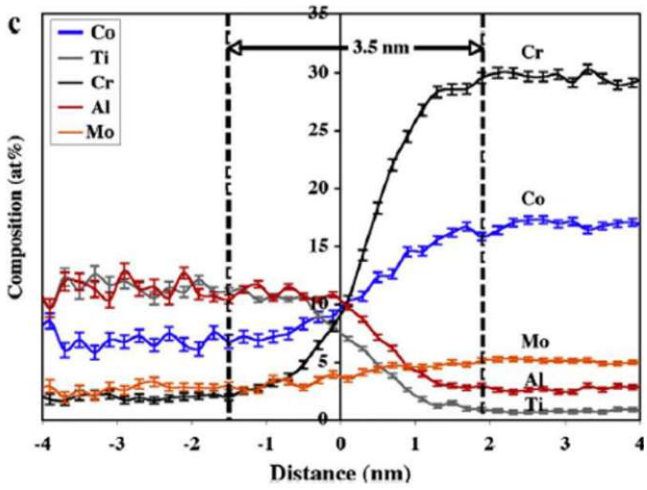

(b)

Figure 39 Comparison of the composition of y' precipitates. Value x=0 corresponds to the interface between matrix and precipitate. Experimental results in the right diagram are taken from [43] and were determined with 3DAP. The left diagram shows the composition of calculated by MatCalc.

The chemical composition for the y' precipitates measured by Singh et al. [42] after cooling is given in Table 13, and the histogram for the calculated Al and Ti content in each size class of the y' precipitate distribution is presented in Figure 40.

Table 13: Chemical composition of y' after WQ

Element	At.-%	Error %
Ti	10.67	1.3
Al	10.49	1.1

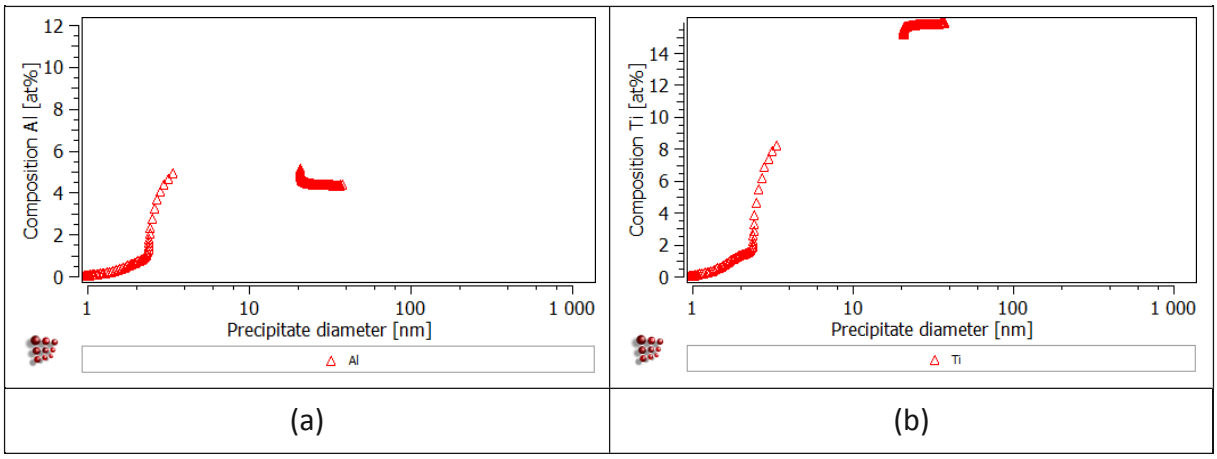

Figure 40 Al and Ti composition of y' precipitates depending on size. After water quenching. Calculated by MatCalc. (a) aluminum; (b) titanium

The simulated primary y' precipitates consist of approx. 4 at.-% of Al and 15 at.-% of Ti, as illustrated in Figure 40. These values differ from the experimental results given in Table 11 However, if an aging time of 50 h is simulated after the cooling procedure, the composition of matrix and precipitation phase show a good agreement with the experimental results (see Figure 39). This means that the simulation deliveres good results, when a near equilibrium condition regarding the precipitate composition is established, which is the case for annealing at 760 °C for 50 h. The results of these simulation the thermodynamic database for nickel, was refined during the Nenimov project.

5.1.2. Study on Rene 65

The improved database was applied for the simulation studies on Rene 65. In Figure 41, the histogram for the calculated size distribution of y' for the slow cooling condition is shown. To illustrate the modifications of thermodynamic database, the simulation results using the

previous and optimized database are compared in Figure 42 for the primary y' size distribution, and in Figure 43 for the secondary y' distribution for different cooling rates. While the primary y' precipitate distribution is in good agreement with experimental data using the previous database, the secondary y' precipitate distribution is shifted to higher sizes by factor of approx. 5. When the optimized database is applied, the calculated mean diameter of these precipitates is close to the experimental data. The experimental data which is used for comparison, was obtained within the Nenimov project.

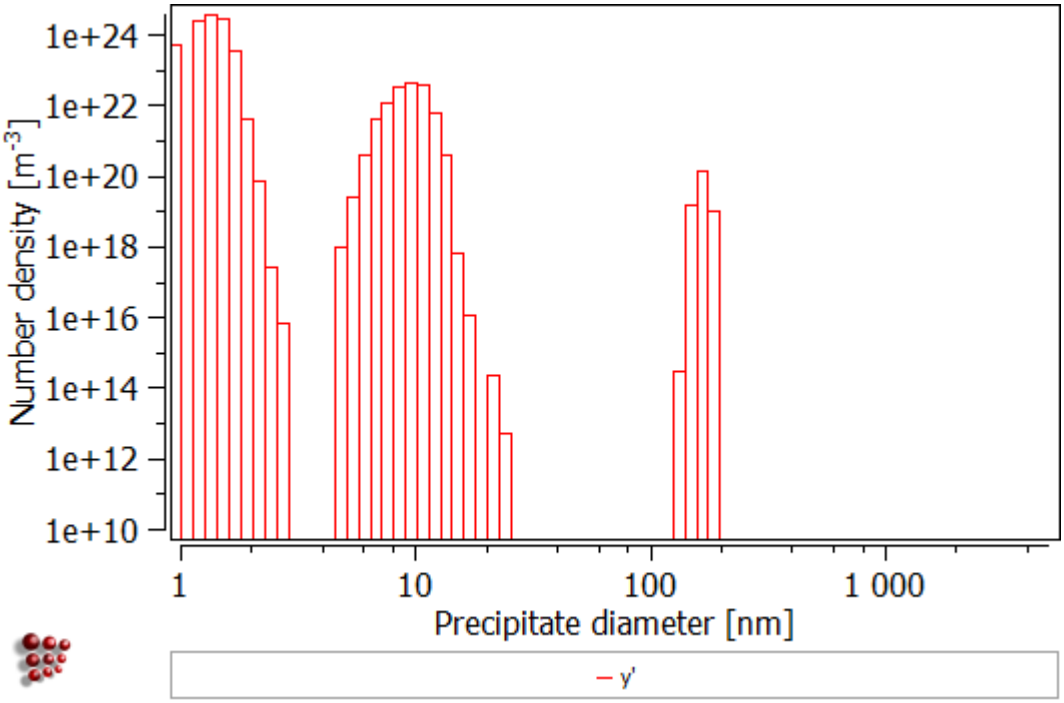

Figure 41: Size distribution of y' after SC calculated by MatCalc "new" database, x-axis: precipitate diameter

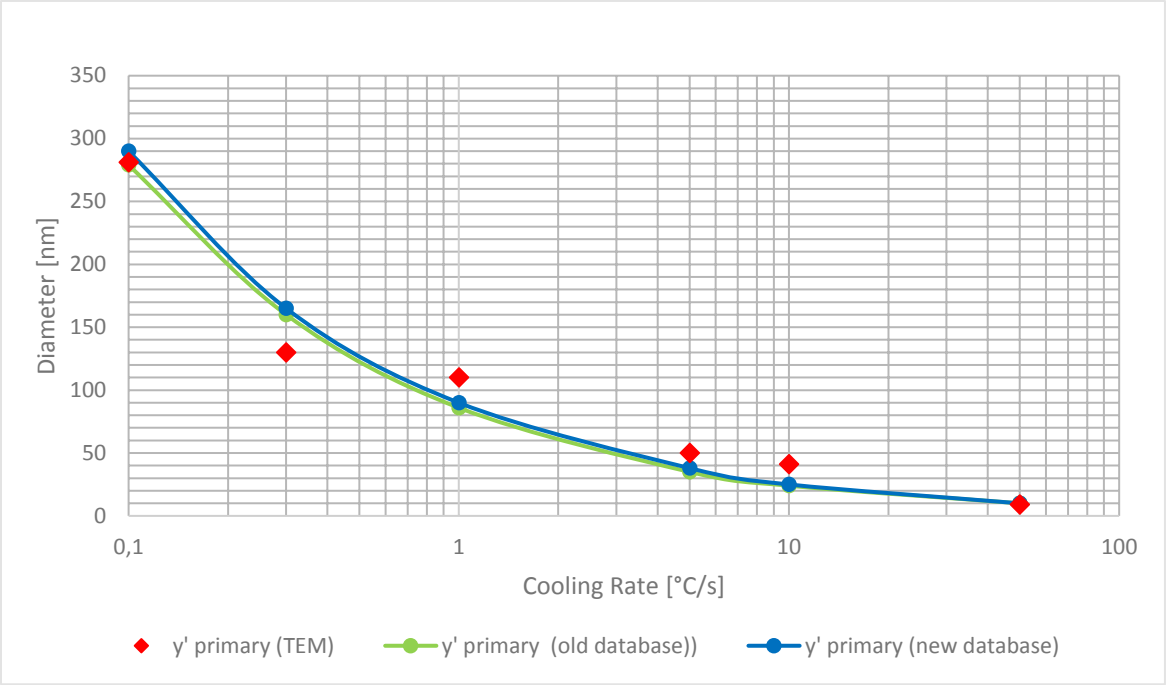

Figure 42: Mean diameter of primary y' precipitates for different cooling rates. Rene 65

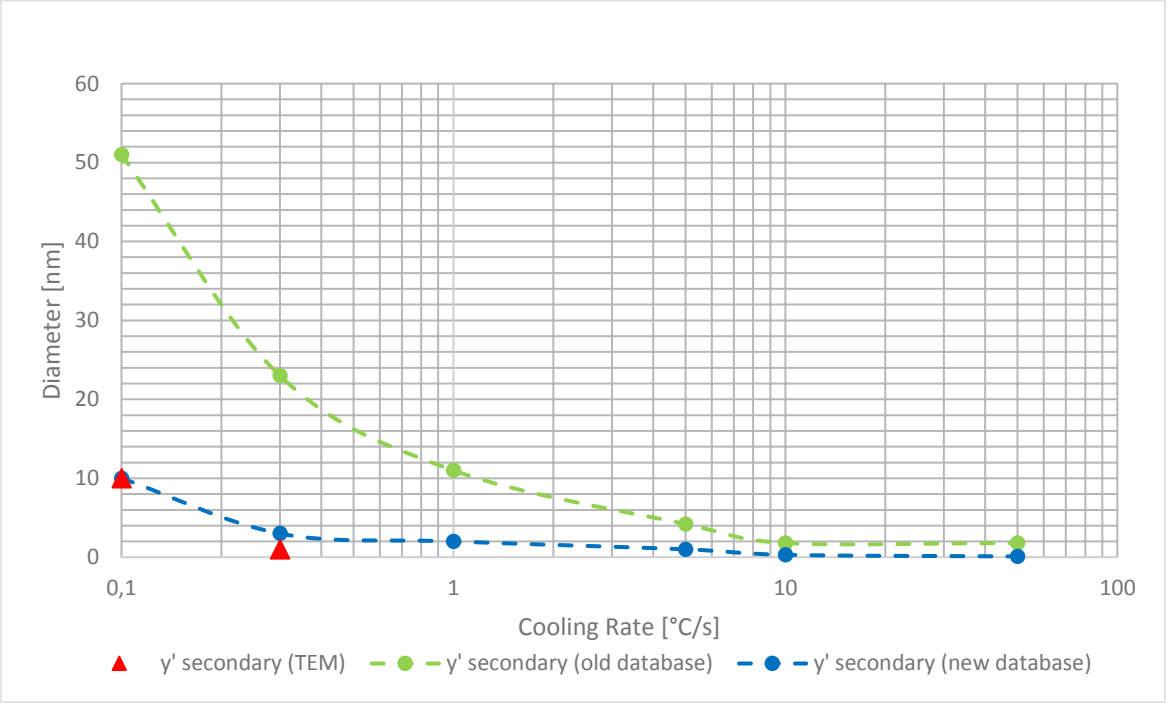

Figure 43: Mean diameter of secondary y' precipitates for different cooling rates. Cropped from Figure 39.

With the optimized database the composition of the y' precipitates is also in good agreement with the experimental values, regarding the Al and Ti content.

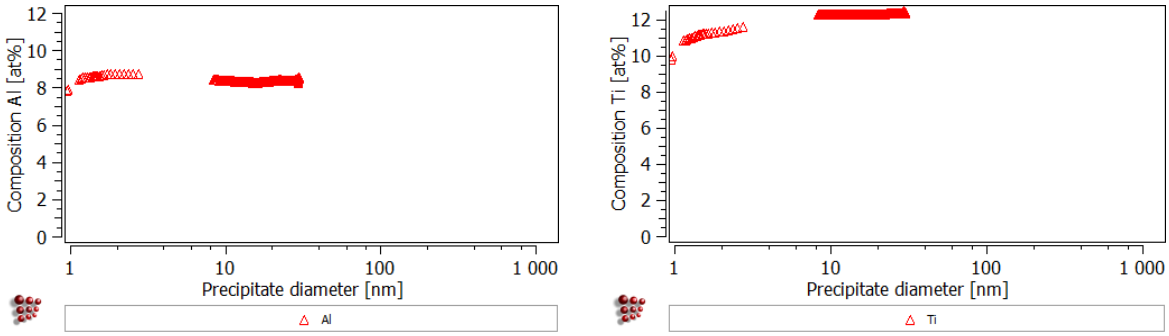

(a) (b)

Figure 44: Chemical composition of y' depending on size, with improved database. After water quenching. (a) aluminum; (b) titanium

The difference in the calculated mean diameter for the secondary y' precipitates, between the previous and optimized database highlights the importance of the thermodynamic database for realistic predictions in precipitation kinetic simulations.

5.1.3. Study on Inconel 718

If the calculated TTP-diagram shown in Figure 25 is compared to an experimentally acquired diagram from Xie et al. [44], which is shown in Figure 45, it is noticed that the temperatures where the phases occur or dissolve are nearly congruent. For the delta phase, even the point of time where it occurs, is similar in the calculated and the measured diagram. The y' and y'' phases seem to emerge earlier in the simulation than in the experiment. An issue that might causes this difference is that in the calculated TTP diagram all precipitates are considered for the calculation of the phase fraction. This means that even very small precipitates with diameters of only a few nanometres (clusters) are taking into account. Precipitates of this size are very difficult to measure with most experimental techniques that are commonly used to determine TTP-diagrams, and would therefore most of the time not be considered in such diagrams, unless they have a sufficient impact on mechanical properties like hardness. Therefore, simulation and experiment should be compared with caution.

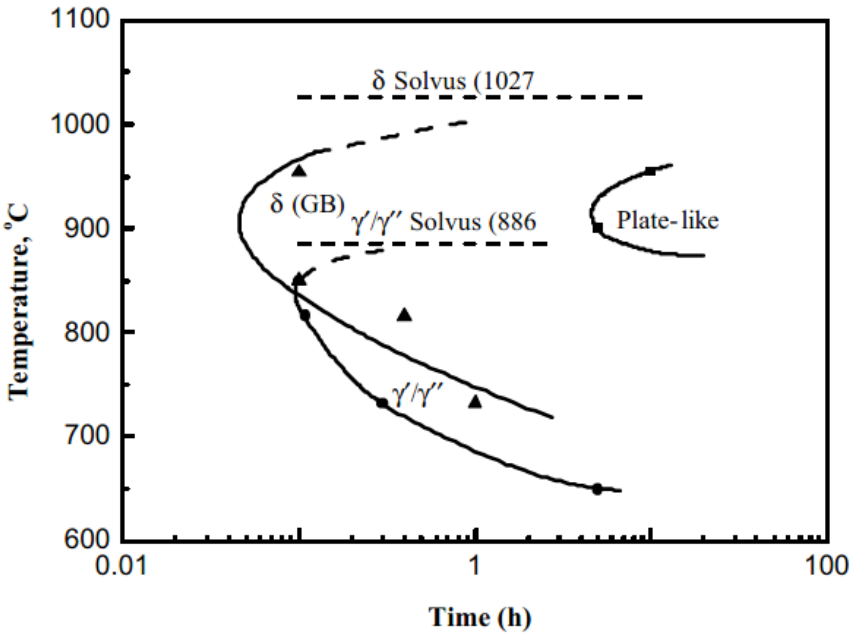

Figure 45: Time-Temperature-Precipitation (TTP) curves for Inconel 718 alloy. [44]

5.2. Microstructure evolution simulation

5.2.1. Work hardening and recovery

The simulation results for the substructure, presented in chapter 4.3.1, seem to be reasonable when compared to experimental, results shown in Figure 46.

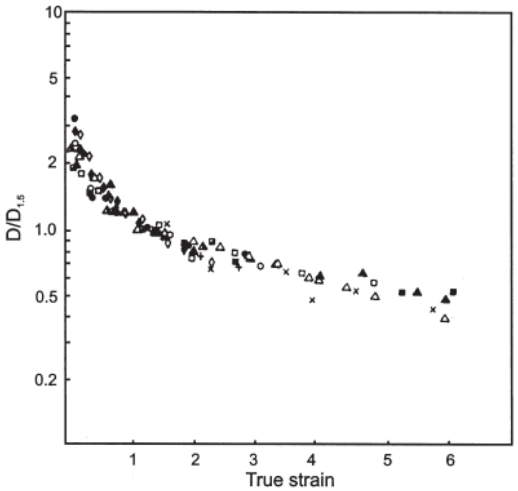

Figure 46: Average cell size as a function of strain for Al, Cu, Fe, Ni, Cr, Nb, (from data assembled by Gil Sevillano et al. (1980) from different authors). The cell size is expressed as a fraction of D1.5, the cell size at a strain of 1.5. [45]

To compare the calculated dislocation densities with experimental data, the increase in strength resulting from an increase in dislocation density was calculated. For this calculation the Taylor equation was used which is explained in chapter 3.1.2. In this equation the pre-factor α was taken to be 0.5 and the Taylor factor was set to M = 3.06. The calculation was carried out within MatCalc. In Figure 47, the calculated results for the work hardening contribution are compared with literature results. The experimental results are taken from Smith et al. [46] for IN-718 and Mittra et al. [47] for IN-626. The IN-625 alloy, was in solution quenched condition and the strain rate applied was 3.0e-4/s while the IN-718 was double aged and a strein rate of 0.1 was applied.

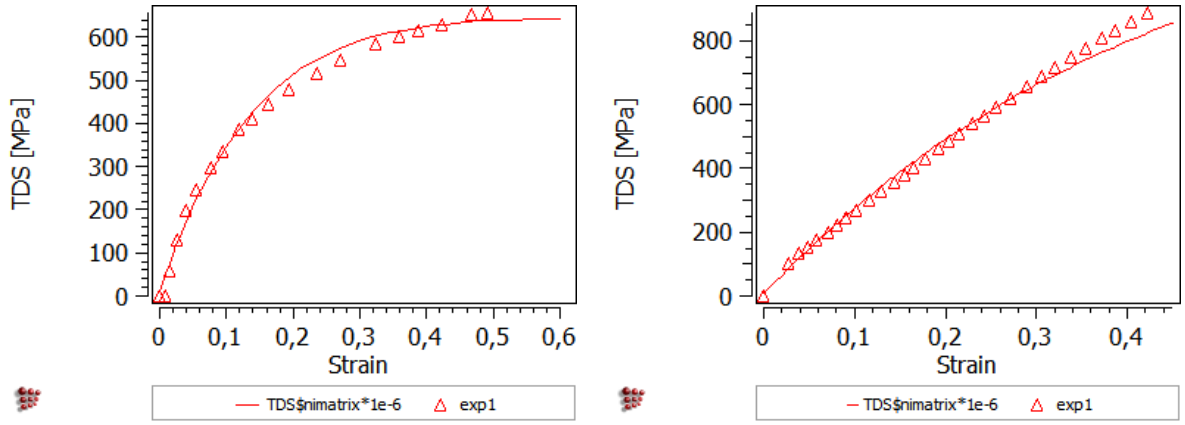

a) IN-718 b) IN-625

Figure 47: Comparison between experimental stress strain data and simulation results. Solid line represents simulation results and data points experimental results.

The simulation results which are presented in Figure 47 show good agreement with the experimental data, but it is important to keep in mind, that some microstructural effects are not considered. The values found for the *A* and *B* parameter should therefore not be taken as rigid values that are correct for every kind of simulation for the same alloy, but have to be reconsidered if there are any factors changed in the simulation. A change in researched process, for example recrystallization evolution instead of strain-hardening or a change in temperature can make it necessary to adjust these parameters. The ABC-model used in this context does not consider a temperature dependency of the A and B parameter.

5.2.2. Dynamic recrystallization (DRX)

The results of the dynamic recrystallization simulation which are shown in chapter 4.3.2 are compared to experimental EBSD data. Experimental results from EBSD measurements for deformation at 980 °C are shown in Figure 48. The blue areas in this figure represent the recrystallized grains. For the case of a true strain level of 0.27, nearly no recrystallization is

noticed, while at a strain level of 0.73 a recrystallized fraction of 15 % is achieved. These values are in good agreement with the recrystallized volume fraction as calculated in the simulations.

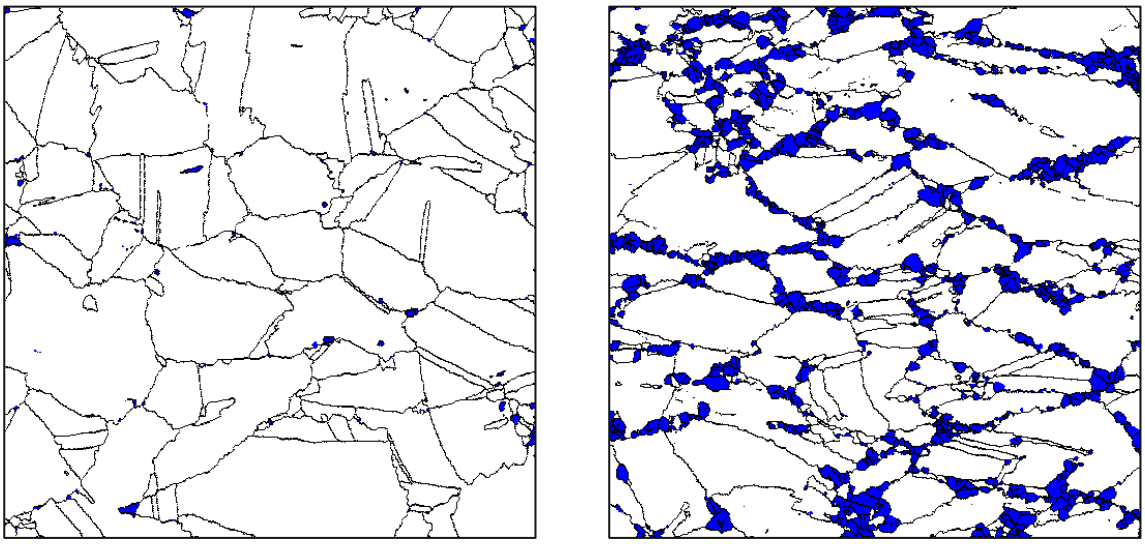

(a) true strain = 0.27 (b) true strain = 0.73

Figure 48: Experimental results from EBSD measurements (map size 200 µm x 200 µm) for deformation at 980°C with a strain rate of 0.1 s^{-1} for a true strain of (a) 0.27, and (b) 0.73. [48]

As shown in Figure 49, it can be recognized that the predicted recrystallized volume fraction for different strain levels is in good agreement with the experimental results determined by EBSD.

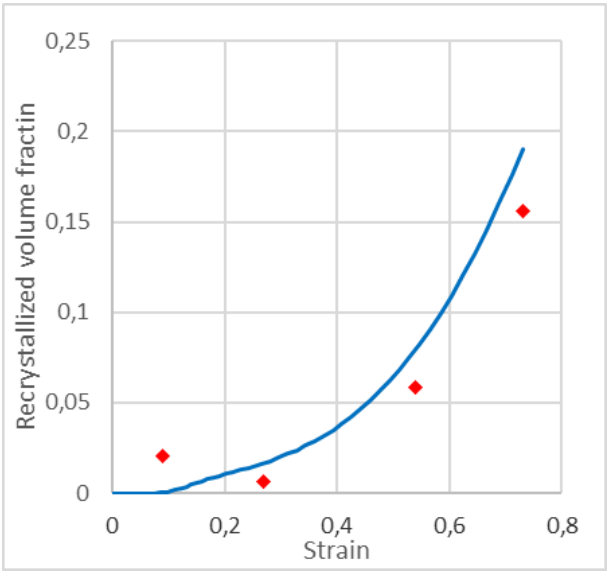

Figure 49: Evolution of recrystallized volume fraction during deformation at 980°C with a strain rate of 0.1 s-1. Solid line symbolizes the simulation and red squares the experimental data.

The grains form the EBSD pictures show a similar behavior although their area based mean grain diameter decreases faster than predicted by the simulation. The measured are based

mean diameter for 0.73 strain is around 25 µm, while the calculated volume based diameter at this point is around 48 µm. The grains in Figure 48(b) show a bimodal size distribution, on the one hand there are the small recrystallized grains and on the other hand the big unrecrystallized grains. The applied single class grain size model for the simulations within this thesis, delivers a number and a volume based mean grain diameter. The volume based mean diameter for a strain of 0.73 is around 48 µm and the number based mean diameter around 8 µm. The area based mean diameter evaluated from EBSD data therefore lies between the calculated volume based and number based diameter. Possible reasons for the gap between measurement and calculation concerning grain diameter are discussed in the following.

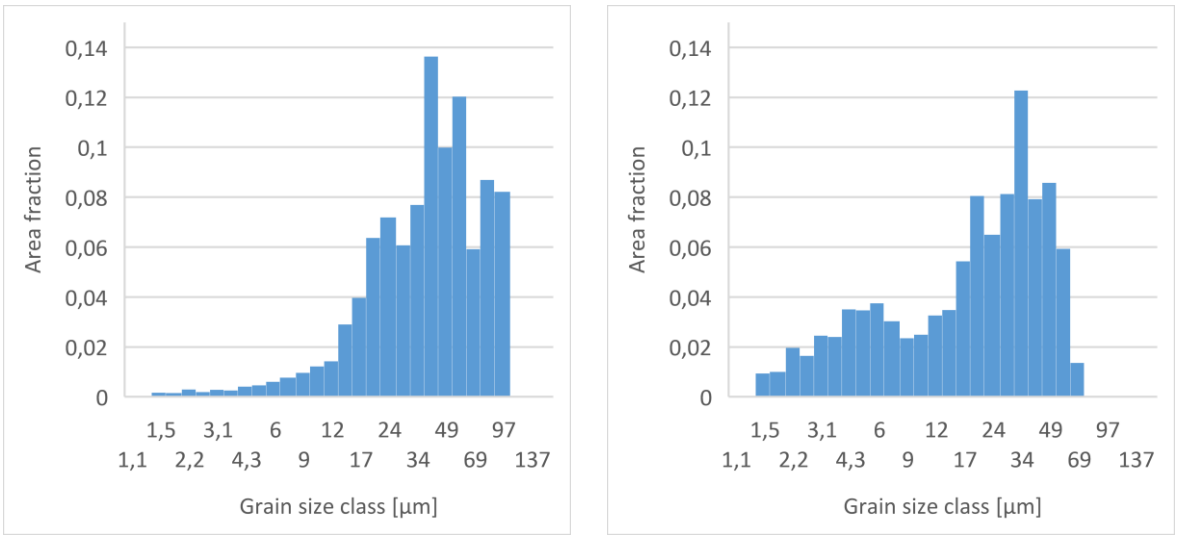

(a) strain=0.27 (b) strain=0.73

Figure 50: grain size class distribution for deformation at 980°C; measured with EBSD; strain rate 0.1 – 1; DRX, (a) strain=0.27; (b) strain=0.73 [48]

The small distribution of grains that occurs around 4 µm at a strain of 0.73, represents recrystallized grains. The shift of the mean value of the unrecrystallized grains from 49 µm at a strain of 0.27 to 34µm at a strain of 0.73 could be an indicator for continuous recrystallization. Therefore, the difference of calculation and measurement may occur due to this effect not being considered within the simulation. To determine the impact of this effect, further research concerning the proportion of continuous and discontinuous recrystallization has to be done. Some approaches to describe continuous dynamic recrystallization numerically are explained Huang and Loge [6]. It is also possible that the difference in the experimental data, concerning unrecrystalized grain size is caused by inhomogeneities in the as received material. Differences in composition or microstructure have a high impact on the microstructural behaviour during recrystallization.

The applied models are not considering every effect that occurs during hot deformation, and not all microstructural dependencies are considered. For example, the influence of deformation velocity (strain rate) is not incorporated in its full meaning. A higher strain rate results in a shorter time for recrystallization in the simulation, but the models does not consider a strain rate dependency of other microstructural processes that could possibly play a role during dynamic recrystallization. The model used for the description of recrystallization is only applicable for discontinuous recrystallization, e.g. recrystallization that occurs due to nucleation and growth. Thus, continuous recrystallization that possibly occurs during the hot deformation of IN-718, may leads to a difference between experimental and simulation results.

5.2.3. Meta-dynamic recrystallization (MDRX)

The results of the meta-dynamic recrystallization simulation shown in 4.3.2, are compared to experimental results derived from EBSD measurements, which are illustrated in Figure 51.

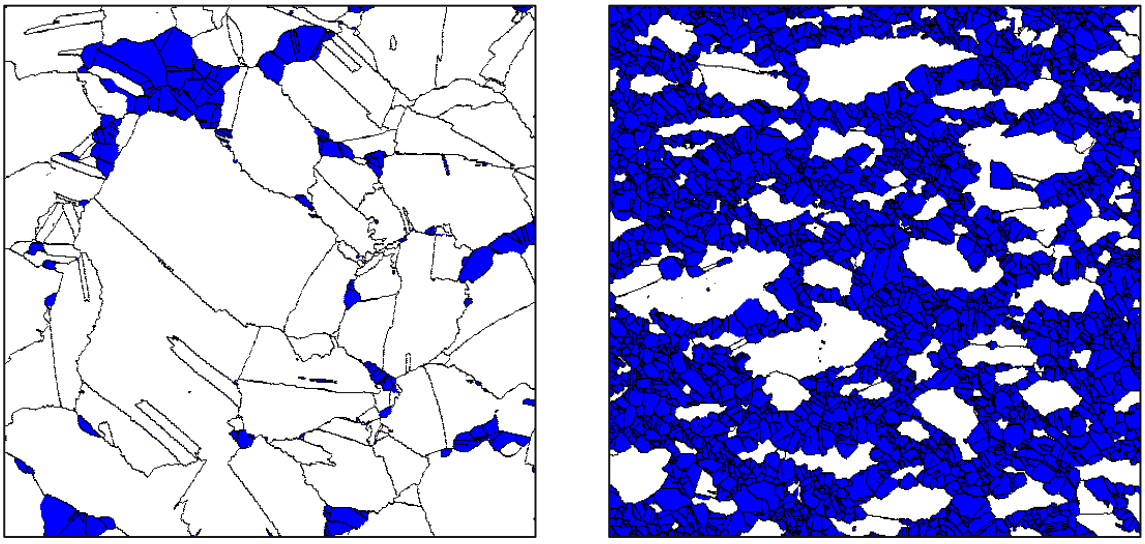

(a) true strain = 0.27 (b) true strain = 0.73

Figure 51: Experimental results from EBSD measurements (map size 200 µm x 200 µm) for deformation at 980 °C with a strain rate of 0.1 s^{-1} and a holding time of 15 s after deformation: (a) true strain of 0.27, and (b) true strain of 0.73. [48]

At a strain level of 0.09 the recrystallization fraction is comparable between experiment and simulation. At a strain levels higher than 0.27 post-recrystallization is more pronounced. The calculated volume fraction of recrystallized grains after 15 s holding time for a strain value of 0.27 is approx. 50 %, which is higher than the experimentally observed value of 10 %. At a strain level of 0.73, the simulation predicts a fully recrystallization microstructure, while in the corresponding EBSD image there are still some unrecrystallized grains present. To summarize these findings, the calculated recrystallized volume fraction increases with time faster than

the corresponding experimental value. This corresponds with the results for the calculated mean grain size which decreases also to fast with time. The calculated mean grain diameters after 15 s are not far of each other either. Although the evolution of the grains over time is not predicted correctly in a quantitative way, it represents the behavioural tendencies of the system concerning recrystallization.

Parameters which influence the post-recrystallization behaviour (MDRX) cannot be adjusted easily because this would also influence the recrystallization behaviour during DRX. Despite of all these factors, the qualitative behaviour of the system is described quite well. A way to further improve the simulation would be to better adjust the grain boundary mobility and their correction factors used within the simulation. Improved models for solute drag and the pinning of grain boundaries by precipitates could also be applied to get more accurate predictions.

6. Summary and Conclusion

In this work, simulation studies have been performed with the software package MatCalc and the corresponding databases to investigate the precipitation and microstructure evolution in different nickel-base superalloys during thermo-mechanical treatment. The findings can be summarized as follows:

Part I: Precipitation kinetics in Nickel-base superalloys

The results for the precipitation kinetics concerning the alloy Rene 65 showed good accordance with experimental data acquired within the Nenimov project. To achieve these results the thermodynamic MatCalc database had to be improved. This improvement was done based on simulation result, which were created during preliminary studies within this thesis. A TTP-Diagram of Inconel 718 was calculated to determine the precipitation kinetics in Inconel 718 alloy.

Part II: Microstructure evolution in Nickel-base superalloys

For the calculation of the grain structure evolution, a coupled simulation has been performed, considering the interaction of precipitates with the microstructural evolution. The DRX simulations for the Inconel 718 alloy, gave nearly the same results as experimental data concerning recrystallized volume fraction. The results of the MDRX simulations were slightly divergent from measured data, but overall the considered microstructural variables, e.g. grain size and recrystallized volume fraction, showed similar behaviour in simulation and experiment.

When all predictions from simulation studies within this thesis are gathered, and interpreted with the necessary knowledge on the simulation process, the microstructural behaviour of nickel based superalloys during heat treatments can be estimated. To achieve simulation results, that produce quantitative accurate values for grain size and the resulting mechanical properties, some further research in the areas of grain boundary mobility model-parameters and recrystallization modelling would be beneficial.

References

[1] M. J. Donachie and S. J. Donachie, *SUPERALLOYS Second Edition*. 2002.

[2] G. E. Dieter, H. a. Kuhn, and S. L. Semiatin, *Handbook of Workability and Process Design*. 2003.

[3] P. Wilson, *Recent Developments in the Study of Recrystallization*. InTech, 2013.

[4] J. W. Christian and S. Mahajan, "Deformation twinning," *Prog. Mater. Sci.*, vol. 39, no. 1–2, pp. 1–157, 1995.

[5] E. Hornbogen, G. Eggeler, and E. Werner, *Werkstoffe - Aufbau und Eigenschaften*. 2008.

[6] K. Huang and R. E. Logé, "A review on dynamic recrystallization phenomena in metallic materials," *Mater. Des.*, vol. 111, no. October, pp. 548–574, 2016.

[7] J. E. Bailey and P. B. Hirsch, "The Recrystallization Process in Some Polycrystalline Metals," *Proc. R. Soc. London A Math. Phys. Eng. Sci.*, vol. 267, no. 1328, pp. 11–30, 1962.

[8] R. Abbaschian and E. Reed-Hill, *Physical Metallurgy Principles*, 4th ed. 2009.

[9] M. Hillert, "On the theory of normal and abnormal grain growth," *Acta Metall.*, vol. 13, no. 3, pp. 227–238, 1965.

[10] E. Kozeschnik, C. Bataille, and K. Janssens, *Modeling solid-state precipitation*. 2012.

[11] B. Sonderegger and E. Kozeschnik, "Generalized nearest-neighbor broken-bond analysis of randomly oriented coherent interfaces in multicomponent Fcc and Bcc structures," *Metall. Mater. Trans. A Phys. Metall. Mater. Sci.*, vol. 40, no. 3, pp. 499–510, 2009.

[12] R. Becker, "Die Keimbildung bei der Ausscheidung in metallischen Mischkristallen," *Ann. der Phys. 32*, vol. 424, no. 1–2, pp. 128–140, 1938.

[13] D. Turnbull, "Impurities and Imperfections," *Am. Soc. Met.*, pp. 121–144, 1955.

[14] B. Sonderegger and E. Kozeschnik, "Interfacial energy of diffuse phase boundaries in the generalized broken-bond approach," *Metall. Mater. Trans. A Phys. Metall. Mater. Sci.*, vol. 41, no. 12, pp. 3262–3269, 2010.

[15] N. Saunders and A. P. Miodownik, *CALPHAD (Calculation of Phase Diagrams): A Comprehensive Guide*. 1998.

[16] K. Wu, F. Zhang, S. Chen, W. Cao, and Y. a. Chang, "A Modeling Tool for the Precipitation Simulations of Superalloys during Heat Treatments," *Superalloys 2008, TMS*, pp. 933–939, 2008.

[17] I. Ansar, "No Title," *Int. Met. Rev.*, vol. 24, no. 20, 1979.

[18] Soon-DonChoi, "Extension of binary analytical equations to ternary ones," vol. 12, no. 1, pp. 25–31, 1988.

[19] E. Nes, "Modelling of work hardening and stress saturation in FCC metals," *Prog. Mater. Sci.*, vol. 41, no. 3, pp. 129–193, 1997.

[20] U. F. Kocks, "Laws for work-hardening and low-temperature creep," *Trans. ASME. Ser. H, J. Eng. Mater. Technol.*, 1976.

[21] P. Sherstnev, P. Lang, and E. Kozeschnik, "Treatment of Simultaneous Deformation and

Solid- State Precipitation in Thermo-Kinetic Calculations," *Eccomas 2012*, no. Eccomas 2012, p. 8, 2012.

[22] H. Buken and E. Kozeschnik, "A Model for Static Recrystallization with Simultaneous Precipitation and Solute Drag," *Metall. Mater. Trans. A Phys. Metall. Mater. Sci.*, vol. 48, no. 6, pp. 2812–2818, 2017.

[23] L. E. Lindgren, K. Domkin, and S. Hansson, "Dislocations, vacancies and solute diffusion in physical based plasticity model for AISI 316L," *Mech. Mater.*, vol. 40, no. 11, pp. 907–919, 2008.

[24] Y. Bergström, "The plastic deformation of metals - a dislocation model and its applicability," *Rev. Powder Metall. Phys. Ceram.*, vol. 2, no. 2 & 3, pp. 79–265, 1983.

[25] F. Roters, D. Raabe, and G. Gottstein, "Work hardening in heterogeneous alloys—a microstructural approach based on three internal state variables," *Acta Mater.*, vol. 48, no. 17, pp. 4181–4189, 2000.

[26] S. Brinckmann, R. Sivanesapillai, and A. Hartmaier, "On the formation of vacancies by edge dislocation dipole annihilation in fatigued copper," *Int. J. Fatigue*, vol. 33, no. 10, pp. 1369–1375, 2011.

[27] M. S. Soliman, E. A. EL-Danaf, and A. A. Almajid, *Effect of heat treatment conditions on the high temperature deformation of 6082-AL alloy*, vol. 83–86. 2010.

[28] G. I. Taylor, "The Mechanism of Plastic Deformation of Crystals. Part I. Theoretical," *Proc. R. Soc. A Math. Phys. Eng. Sci.*, vol. 145, no. 855, pp. 362–387, 1934.

[29] Y. Huang and F. J. Humphreys, "Subgrain growth and low angle boundary mobility in aluminium crystals of orientation {110}〈001〉," *Acta Mater.*, vol. 48, no. 8, pp. 2017–2030, 2000.

[30] D. G. Cram, H. S. Zurob, Y. J. M. Brechet, and C. R. Hutchinson, "Modelling discontinuous dynamic recrystallization using a physically based model for nucleation," *Acta Mater.*, vol. 57, no. 17, pp. 5218–5228, 2009.

[31] W. T. Read and W. Shockley, "Dislocation Models of Crystal Grain Boundaries," *Phys. Rev.*, vol. 78, pp. 275–289, 1950.

[32] Y. Estrin, L. S. Tóth, A. Molinari, and Y. Bréchet, "A dislocation-based model for all hardening stages in large strain deformation," *Acta Mater.*, vol. 46, no. 15, pp. 5509–5522, 1998.

[33] E. Nes, "Modelling of work hardening and stress saturation in FCC metals," *Prog. Mater. Sci.*, vol. 41, no. 3, pp. 129–193, 1997.

[34] D. Turnbull, "Theory of grain boundary migration rates," *Trans. AIME J. Met.*, vol. 3, no. 8, pp. 661–665, 1951.

[35] M. Maalekian, R. Radis, M. Militzer, A. Moreau, and W. J. Poole, "In situ measurement and modelling of austenite grain growth in a Ti/Nb microalloyed steel," *Acta Mater.*, vol. 60, no. 3, pp. 1015–1026, 2012.

[36] H. S. Zurob, Y. Brechet, and G. Purdy, "A model for the competition of precipitation and recrystallization in deformed austenite," *Acta Mater.*, vol. 49, no. 20, pp. 4183–4190, 2001.

[37] E. Nes, "The Effect of a Fine Particle Dispersion on Heterogeneous," vol. Vol. 24, pp. 391–398, 1976.

[38] M. Rath and E. Kozeschnik, “Coupled Grain Growth and Precipitation Modeling in Multi-Phase Systems,” *Mater. Sci. Forum*, vol. Vol. 753, pp. 357–360, 2013.

[39] Y. Yazawa, T. Furuhara, and T. Maki, “Effect of matrix recrystallization on morphology, crystallography and coarsening behavior of vanadium carbide in austenite,” *Acta Mater.*, vol. 52, no. 12, pp. 3727–3736, 2004.

[40] A. R. Jones and B. Ralph, “The influence of recrystallization on carbide particle distributions in a fully stabilized austenitic steel,” *Acta Metall.*, vol. 23, no. 3, pp. 355–363, 1975.

[41] J. W. Cahn, “The impurity-drag effect in grain boundary motion,” *Acta Metall.*, vol. 10, no. 9, pp. 789–798, 1962.

[42] A. R. P. Singh *et al.*, “Influence of cooling rate on the development of multiple generations of γ′ precipitates in a commercial nickel base superalloy,” *Mater. Charact.*, vol. 62, no. 9, pp. 878–886, 2011.

[43] J. Tiley, G. B. Viswanathan, R. Srinivasan, R. Banerjee, D. M. Dimiduk, and H. L. Fraser, “Coarsening kinetics of γ′ precipitates in the commercial nickel base Superalloy René 88 DT,” *Acta Mater.*, vol. 57, no. 8, pp. 2538–2549, 2009.

[44] X. Xie, C. Xu, G. Wang, J. Dong, W. D. Cao, and R. Kennedy, “Ttt Diagram of a Newly Developed Nickel-Base Superalloy - Allvac® 718Plus™,” *Superalloys 718, 625, 706 Deriv.*, pp. 193–202, 2005.

[45] F. J. Humphreys and M. Hatherly, “Recrystallization and related annealing phenomenon,” *Elsevier*, p. 710, 2004.

[46] D. H. Smith *et al.*, “Microstructure and mechanical behavior of direct metal laser sintered Inconel alloy 718,” *Mater. Charact.*, vol. 113, pp. 1–9, 2016.

[47] J. Mittra, J. S. Dubey, U. D. Kulkarni, and G. K. Dey, “Role of dislocation density in raising the stage II work-hardening rate of Alloy 625,” *Mater. Sci. Eng. A*, vol. 512, no. 1–2, pp. 87–91, 2009.

[48] M. Rath, “Unpublished manuscript,” TU WIEN.

List of figures

Figure 1: Production routes for nickel-base superalloys. 6

Figure 2 Schematic illustration of major operations used for ingot breakdown [1] 7

Figure 3: microscope images of as received material; polished and etched. 7

Figure 4: Effect of microstructural mechanisms on the flow curve (a) recovery, and (b) recrystallization. [3] 9

Figure 5: A dislocation that is pinned at two points (for example at precipitates) becomes a "frank read source" at a certain stress level (τQ). [5] 10

Figure 6: Recovery of defects (annihilation), a: interstitial atom reacts with vacancy; b: line dislocations with opposite burgers vector directions react with each other. [5] 11

Figure 7: Rearrangement of defects. A: vacancies form "dislocation-ring"; b: Dislocations annihilate and form LAGB. [5] 11

Figure 8: Different types of DRX [6] 12

Figure 9: The bulge mechanism for the formation of a nucleus at a grain boundary. [8] 13

Figure 10: Effect of processing parameters on flow stress. [6] 14

Figure 11: Effect of processing parameters on recrystallized volume fraction. [6] 15

Figure 12: Effect of processing parameters on grain size evolution. [6] 15

Figure 13: Schematic representation of a B-rich spherical precipitate growing in a supersaturated matrix. [10] 18

Figure 14: Time integration of the evolution equations as implemented in MatCalc. [10] 20

Figure 15: Deformation stages in polycrystalline fcc metals: (a) schematic stress-strain curves, and (b) strain hardening (Θ) vs shear tress (τ) curves. [19] 24

Figure 16: The subgrain size distribution within each grain of average radius r. The shaded area represents the fraction of subgrains larger than the critical size rc. [30] 27

Figure 17: Screenshot from MatCalc; thermo-mechanical treatments window. 36

Figure 18: Calculated equilibrium phase diagram for Rene 65. 37

Figure 19: Temperature, phase fraction, mean diameter and number density of y' precipitates dependent on time. Cooling rate 50°C/s 38

Figure 20: Temperature, phase fraction, mean diameter and number density of y' precipitates dependent on time. Cooling rate 50°C/s 39

Figure 21: y' precipitate size distribution at 50°C/s cooling rate. x-axis shows diameter and y-axis number density. 39

Figure 22: y' precipitate size distribution at 0,1°C/s cooling rate. x-axis shows diameter and y-axis number density. 40
Figure 23: Calculated stable phase diagram for IN-718. 41
Figure 24: Calculated metastable phase diagram for IN-718. 42
Figure 25: Calculated TTP-diagram for IN-718 42
Figure 26: Evolution of (a) dislocation density and (b) subgrain diameter with true strain. 43
Figure 27: Heat treatment for DRX and MDRX simulation 44
Figure 28: Precipitation distribution imported into MatCalc at the beginning of the simulation. 45
Figure 29: Evolution of precipitates during annealing. 46
Figure 30: Evolution of recrystallized volume fraction during deformation at 980 °C and 1020 °C with a strain rate of 0.1 s^{-1} (DRX) 47
Figure 31: Evolution of mean grain diameter (area based) during deformation at 980 °C and 1020 °C with a strain rate of 0.1 s^{-1} (DRX) 47
Figure 32: Evolution of recrystallized volume fraction for different true strain level for holding at 980 °C (MDRX). 48
Figure 33: Evolution of recrystallized volume fraction for different true strain level for holding at 1020 °C (MDRX). 49
Figure 34: Evolution of the mean grain diameter (area based) for different true strain level for holding at 980 °C (MDRX) 49
Figure 35: Evolution of the mean grain diameter (area based) for different true strain level for holding at 1020 °C (MDRX) 50
Figure 36: Schematic illustrating the effect of cooling rate on the formation of different generations of y' precipitates.[42] 51
Figure 37 Energy- filtered transmission electron microscopy images obtained using Cr M-edge in the electron energy-loss spectroscopy spectrum from solutionized and slow cooled samples (SC). 52
Figure 38: Size distribution of y' after SC calculated by MatCalc “old” database, x-axis: precipitate diameter 53
Figure 39 Comparison of the composition of y' precipitates. Value x=0 corresponds to the interface between matrix and precipitate. Experimental results in the right diagram are taken from [43] and were determined with 3DAP. The left diagram shows the composition of calculated by MatCalc. 54
Figure 40 Al and Ti composition of y' precipitates depending on size. After water quenching. Calculated by MatCalc. (a) aluminum; (b) titanium 54

Figure 41: Size distribution of y' after SC calculated by MatCalc “new” database, x-axis: precipitate diameter 55

Figure 42: Mean diameter of primary y' precipitates for different cooling rates. Rene 65 56

Figure 43: Mean diameter of secondary y' precipitates for different cooling rates. Cropped from Figure 39. 56

Figure 44: Chemical composition of y' depending on size, with improved database. After water quenching. (a) aluminum; (b) titanium 57

Figure 45: Time-Temperature-Precipitation (TTP) curves for Inconel 718 alloy. [44] 58

Figure 46: Average cell size as a function of strain for Al, Cu, Fe, Ni, Cr, Nb, (from data assembled by Gil Sevillano et al. (1980) from different authors). The cell size is expressed as a fraction of D1.5, the cell size at a strain of 1.5. [45] 58

Figure 47: Comparison between experimental stress strain data and simulation results. Solid line represents simulation results and data points experimental results. 59

Figure 48: Experimental results from EBSD measurements (map size 200 µm x 200 µm) for deformation at 980°C with a strain rate of 0.1 s^{-1} for a true strain of (a) 0.27, and (b) 0.73. [48] 60

Figure 49: Evolution of recrystallized volume fraction during deformation at 980°C with a strain rate of 0.1 s-1. Solid line symbolizes the simulation and red squares the experimental data.60

Figure 50: grain size class distribution for deformation at 980°C; measured with EBSD; strain rate 0.1 – 1; DRX, (a) strain=0.27; (b) strain=0.73 [48] 61

Figure 51: Experimental results from EBSD measurements (map size 200 µm x 200 µm) for deformation at 980 °C with a strain rate of 0.1 s^{-1} and a holding time of 15 s after deformation: (a) true strain of 0.27, and (b) true strain of 0.73. [48]..... 62